Combustion behavior of single iron particles

Applications in Energy and Combustion Science 14 (2023) 100145

Contents lists available at ScienceDirect

Applications in Energy and Combustion Science

journal homepage: www.elsevier.com/locate/jaecs

Combustion behavior of single iron particles, Part II: A theoretical analysis based on a zero-dimensional model

Aki Fujinawa [a], Leon C. Thijs [b], Joel Jean-Philyppe [a], Aidin Panahi [c,d], Di Chang [d], Martin Schiemann [e], Yiannis A. Levendis [d], Jeffrey M. Bergthorson [a], XiaoCheng Mi [b,f,*]

[a] Department of Mechanical Engineering, McGill University, Montreal, QC, Canada
[b] Department of Mechanical Engineering, Eindhoven University of Technology, Eindhoven, The Netherlands
[c] Department of Mechanical Engineering, Massachusetts Institute of Technology, Cambridge, MA, USA
[d] Mechanical and Industrial Engineering, Northeastern University, Boston, MA, USA
[e] Department of Energy Plant Technology, Ruhr-University Bochum, Bochum, Germany
[f] Eindhoven Institute of Renewable Energy Systems, Eindhoven University of Technology, Eindhoven, The Netherlands

ARTICLE INFO

Keywords:
Iron particle
Metal fuel
Heterogeneous combustion
Droplet combustion

ABSTRACT

Following the ignition and solid-to-liquid phase transition of a fine (on the order of 10–100 μm in diameter) iron particle, the self-sustained combustion of a liquid-phase droplet of iron and its oxides takes place. The objective of the current work is to develop an interpretive and explanatory model for the liquid-phase combustion of a single fine iron particle. A zero-dimensional physicochemical model is developed assuming fast internal processes, such that the combustion rate is limited by the rate of external oxygen (O_2) transport. The model considers a particle covered by a shell of liquid-phase FeO enclosing a core of liquid-phase Fe. Stefan flow and diffusion are considered for the gas-transport of O_2, while the gas-transport of gas-phase Fe and FeO are calculated via diffusion only. The outward gas-phase Fe and FeO consume inward-transported O_2 to stoichiometrically form hematite (Fe_2O_3), and the remaining oxygen that reaches the particle surface is entirely consumed to form liquid-phase FeO. The time history of simulated particle temperature shows consistent overprediction of the peak particle temperature when compared to experimental temperature measurements, indicating that the assumption of fast internal kinetics may be incorrect. The model is also unable to capture the apparent slow cooling rate observed in experiments. A further analysis is performed through a heuristic model with a calibrated reaction-rate law, where the internal diffusion of reactive Fe and O ions may become rate-limiting. The calibration of the pre-exponential factor in the Arrhenius term to match the experimental peak temperature yielded good agreement of time to peak temperature, as well as the slow cooling rate. The heuristic model considering internal diffusion predicts a plateau in peak temperature with increasing oxygen concentration. Possible uncertainties of the models, as well as future work, are discussed.

1. Introduction

To mitigate further global climate change, current energy systems must transition away from fossil fuels. This calls for the urgent development of clean and efficient energy carriers that can store and transport renewable energy. Iron is an excellent candidate, given its carbon-free nature and high energy density [1–3]. The combustion of iron particles results in the formation of condensed-phase iron oxides, which can be collected and reduced back into pure iron powder using green hydrogen [4]. As iron exhibits flame temperatures comparable to that of hydrocarbons, existing fossil fuel power plants can be retrofitted for iron, making iron fuel a unique and promising future energy carrier [5].

Recent experimental studies on single iron particle combustion have provided temporally-resolved particle temperature measurements in air with varying oxygen concentrations. The time history of particle temperature in ambient air has been provided by Ning et al. [6]. Part I of this paper by Panahi et al. [7] reports the time history of particle temperature in high gas temperatures in 21% O_2, 50% O_2, and pure O_2. These experimental measurements allow for an enhanced fundamental understanding of the mechanism of single iron particle combustion, while also providing a benchmark for model validation. This work presents the development of a numerical model based on a zero-dimensional framework, validated against the aforementioned

* Corresponding author at: Department of Mechanical Engineering, Eindhoven University of Technology, Eindhoven, The Netherlands.
E-mail address: x.c.mi@tue.nl (X. Mi).

https://doi.org/10.1016/j.jaecs.2023.100145
Received 15 July 2022; Received in revised form 2 May 2023; Accepted 15 May 2023
Available online 25 May 2023

set of experimental measurements, to provide a more in-depth theoretical analysis of the dynamics and mechanisms of single iron particle combustion.

The combustion of an iron particle begins with solid-phase ignition, where the oxidation rate is exponentially dependent on particle temperature and inversely proportional to the thickness of the growing oxide layer. This process is well understood, given an abundance of literature from the metallurgical field on the solid-phase oxidation of iron [8–13], and recent computational studies on the ignition characteristics of iron particles [14,15]. The many outstanding unknowns of iron oxidation lie in temperatures where iron and its oxide products exist in liquid-phase. In particular, there is no experimental literature on the chemical kinetics of liquid-phase iron particle oxidation, or any quantitative understanding of the dynamic composition of reacting molten iron droplets. The poor understanding of the heat release rate during liquid-phase iron particle combustion renders the development of efficient, large-scale energy-conversion technologies for iron fuel difficult. These knowledge gaps hinder our abilities to drive the development of iron fuel as a clean and recyclable energy carrier [16].

Despite the lack of extensive fundamental studies on the combustion of liquid-phase iron particles, there is an array of experimental literature on the mechanisms behind molten iron oxidation, which arose owing to interest in the steelmaking industry. Initial rate-limiting mechanism analysis of the oxidation of liquid iron in pure oxygen was conducted by Emi et al. [17] and Banya and Shim [18]. An experimental setup consisting of a cm-scale magnesia crucible was used, where an electrolytic iron sample was melted in an inert atmosphere. Upon filling the reaction chamber with oxygen to around 1 atmosphere (atm), the pressure in the chamber was recorded to probe the rate of oxidation. Analysis indicated that, following the rapid oxidation of the iron melt, the rate of oxidation markedly slows down due to the formation of an oxide layer, where the oxidation becomes limited by the diffusion transport of oxygen ions through the oxide layer.

A large set of metallurgical literature on molten iron rod combustion is also available, owing to research efforts that stemmed from interest in flammability of iron rods from a fire safety and explosion hazard standpoint. Phenomenological information can be extracted from this experimental literature to better understand the possible mechanisms behind liquid-phase iron combustion. A mm-diameter iron rod is typically heated from one end, where a molten droplet of iron and its oxides develop at the heated region. This reaction front continues to melt and propagate further down the rod [19]. This combustion process gives rise to distinct, multi-phase layers of molten oxides, molten unoxidized iron, and thermally unaffected iron [20]. Early experimental investigations by Sato et al. [19] and Hirano et al. [21] showed that the rate-limiting mechanism was likely the adsorption of gaseous oxygen at the oxide melt/gas interface. Subsequent experiments by Steinberg et al. [22,23] in high pressure oxygen exhibited excess oxygen above the stoichiometric requirement to form the highest oxidized product of iron, hematite (Fe_2O_3), in the product oxide melt. This finding suggested the rate-limiting mechanism to be the kinetic reaction at the pure iron/oxide melt interface. Dreizin [24] reconciled this apparent disagreement in experimental literature on the rate-limiting mechanism of molten iron-rod combustion, elucidating that the limiting rate can either be internal iron oxidation kinetics at sufficiently high gas temperatures [22,23,25], or the rate of gaseous oxygen incorporation at lower gas temperatures [19,21].

Further experimental studies by Muller et al. [26] explored the mixed molten droplet that forms during the laser ignition of iron rods in oxidizing environments. A pure iron sample quenched in water post-combustion revealed a spatially non-uniform distribution of iron, oxides, microporosities, and mm-scale gas bubbles in the expanded droplet attached to the rod [26]. This work is consistent with the findings of Steinberg et al., where excess oxygen was found in the iron and oxide melt [22]. Muller et al. [26] also identified a transition temperature (around 2350 K) at which distinct layers of molten iron/oxides overcome the miscibility barrier and begin to mix.

To understand the potential implications of these findings to iron particle combustion, one must reconcile the fundamental differences between iron rod and iron particle combustion. In mm-scale diameter rods, there is a temperature gradient from the heated location to the solid rod. Distinct, multi-phase layers of iron and its oxides that form [20] also give rise to a spatial gradient in species concentration. In micron-sized particles, the Biot number is much less than unity [14], indicating a uniform temperature in the entire particle. The miscibility of molten layers of iron and iron oxides in particle combustion is unknown, and will require further experimental exploration of the composition of burning molten iron droplets. The evidence for excess oxygen dissolved into the molten oxide layer in iron-rod experiments is directly relevant to iron particle combustion. Recent studies on the morphology of a burning iron particle show the presence of non-uniform holes, through which excess absorbed O_2 appears to escape from the particle upon cooling and re-solidification [27,28]. Moreover, single particle combustion studies by Ning et al. [6] and Panahi et al. [7] show a second peak in particle temperature near the solidification point of magnetite (Fe_3O_4), known as the shoulder of the spearpoint [29]. Ning et al. [6] speculate this to be due to a sudden crystallization/solidification of a supercooled droplet of molten iron oxide with high O content, comparable to that of Fe_3O_4.

Alas, the quantitative analysis from presently available molten iron combustion literature cannot be directly applied to iron particle combustion due to the intrinsic complexities of sample geometry and experimental conditions involving high oxygen pressures. A number of recent studies have focused on single particle combustion [6,7,30–32], however, no extensive quantitative analysis on the internal kinetics of a burning molten droplet, or the composition of such a droplet, was made. While further experimental campaigns are certainly necessary to fully elucidate the governing physics of iron particle combustion in liquid-phase, reasonable inferences can be made to model the process approximately. As condensed-phase kinetics of iron oxidation likely become sufficiently fast at elevated temperatures (i.e., when the iron particle becomes fully molten at $T_p = 1870$ K), the rate of liquid-phase iron oxidation is likely limited by the external-O_2-transport rate [14]. While there is no quantitative information on the composition of a reactive molten droplet of iron, Fe_2O_3 is unstable above its melting point, and thermo-chemical equilibrium suggests that the liquid-phase oxide can have an oxidation stage up to the stoichiometric molar ratio of Fe_3O_4, corresponding to around $Z_O = 0.57$, where $Z_O = O/(Fe + O)$ describes the elemental mole fraction of oxygen in the particle.

The current work presents the development of an interpretive model for the liquid-phase combustion of an iron particle, based on the simplifying assumptions that the rate of external oxidizer transport is rate limiting, and the liquid-phase particle reaches an oxidation state of $Z_O = 0.5$ (the stoichiometry of "liquid-phase FeO") in liquid-phase. The paper is structured in the following manner. An overview of the thermodynamics of the iron/oxygen system is presented, where an approximate combustion mechanism is postulated. The model formulation for the combustion of a single iron particle is presented in detail, with a brief description of the solid-phase oxidation and phase transition model, followed by the formulation of the liquid-phase combustion model. Simulation results for combustion in air with varying oxygen concentrations and gas temperatures are compared to experimental measurement. A further analysis through a heuristic model is proposed, to illustrate the possible rate-limiting physics. A parametric analysis and discussion of results are presented. Concluding remarks are given.

2. Thermodynamics of the Fe-O system

Thermodynamic data and equilibrium calculations can elucidate the stable composition of a binary iron/oxygen (hereinafter referred to as Fe-O) system.

Fig. 1 presents the Fe-O phase diagram, constructed by phase equilibrium boundaries based on thermodynamic data of various species

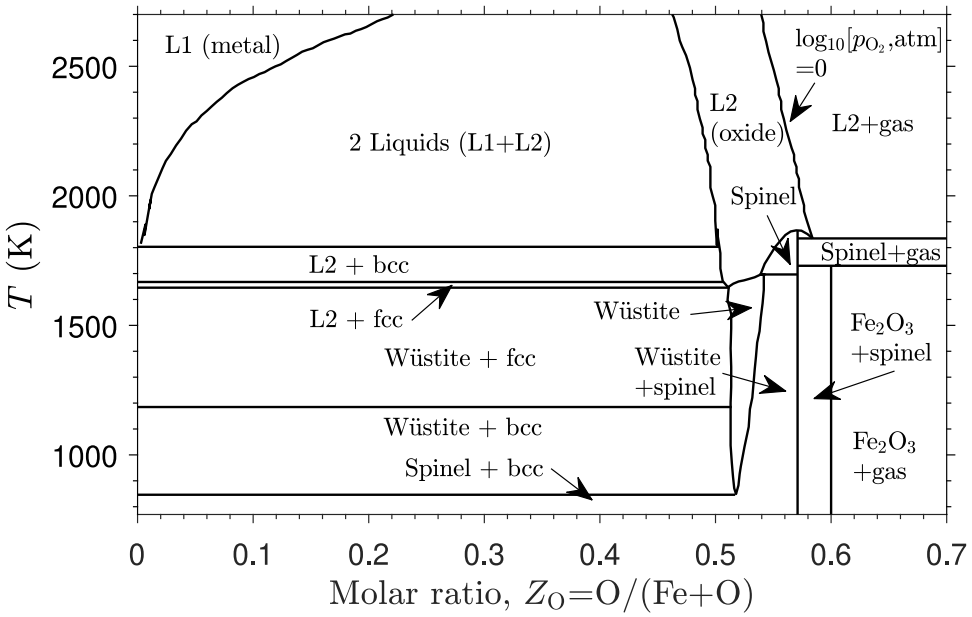

Fig. 1. Fe-O phase diagram based on data from [33]. Wüstite refers to solid-phase FeO, spinel refers to solid-phase Fe_3O_4, while bcc and fcc refer to body centered cubic and face centered cubic structures of Fe, respectively. L1 (metal) describes liquid-phase Fe and L2 (oxide) describes liquid-phase iron oxide.

that may exist in an Fe-O system. As the rates of oxidation of Fe to FeO, Fe_3O_4, and Fe_2O_3 are finite, a burning iron particle is at thermodynamic non-equilibrium during its combustion. Therefore, a given state of a burning particle is rate-dependent and is unlikely to be attributed to a unique location in the phase diagram. However, information from thermodynamic equilibrium calculations can provide critical insight on favored species and possible compositions of a burning droplet of iron and its oxides. The general trajectory of the combustion of a liquid-phase iron particle can be speculated to be within the 2 Liquids dome (also referred to as L1+L2), given the high particle temperature and intermediate molar ratio of O to Fe atoms. While the exact composition of species in the liquid-phase regions is unknown, the 2 Liquids region is a mixture of iron and oxide species in liquid phase, of increasing oxide content as the particle intakes more gaseous oxidizer (increasing molar ratio $Z_O = O/(Fe + O)$). The right boundary of the 2 Liquids region roughly corresponds to an O/(Fe+O) molar ratio of $Z_O = 0.5$, or that of stoichiometric FeO. The curvature of this boundary is likely due to the presence of non-stoichiometric compounds of FeO at high temperatures. The neighboring region to the right of the boundary consists only of L2 (oxide) phase, suggesting that when an Fe-O system in liquid-phase reaches a molar ratio of approximately 0.5, it is void of L1 (metal) or pure iron. This indicates that a liquid-phase iron particle undergoing combustion will likely oxidize to an oxidation state of $Z_O = 0.5$, until all Fe is consumed.

The L2 (oxide) region extends to approximately the O/(Fe+O) molar ratio of $Z_O = 0.57$ for an oxygen pressure of 1 atm. This region shares a boundary with the L2+gas region, where the molten oxide phase becomes saturated and is unable to absorb additional gaseous oxidizer. The location of the boundary (and its corresponding molar ratio) is strongly dependent on the oxygen pressure, suggesting that the extent of oxidation a molten iron particle can reach depends on the gas pressure of the environment. While not explicitly illustrated in Fig. 1, it can be speculated that, for oxygen pressures higher than 1 atm, this boundary will be located at a molar ratio beyond that of stoichiometric Fe_2O_3, which reconciles the absorption of oxygen in the molten oxide phase beyond the amount required for stoichiometric Fe_2O_3 in the iron rod experiments at high oxygen pressures [22,23]. Moreover, this suggests that the consideration of excess oxygen absorption beyond the stoichiometric requirement to form Fe_2O_3 is not necessary to model the combustion of iron particles at ambient pressure conditions in air.

It is critical to note that Fe_3O_4 (and Fe_2O_3) are crystalline structures that are only stable in the solid phase. While experimental findings suggest re-solidified combustion products to be mainly composed of Fe_3O_4 and Fe_2O_3 [28,34], the formation of such crystal structures most likely occurs subsequent to the re-solidification and further cooling. While the L2 (Oxide) region of the Fe-O phase diagram suggests liquid-phase iron-oxygen systems may have an O/(Fe+O) molar ratio corresponding to a value higher than that of stoichiometric FeO, it is unknown whether further heat release upon reaching an Fe-O ratio above 0.5 can occur in liquid-phase, or only upon re-solidification of the particle. This paper, therefore, explores a model in which only the oxidation to $Z_O = 0.5$ is considered during the liquid-phase combustion of the iron particle. The following mechanism for liquid-phase iron particle combustion is considered:

1. The particle intakes gas-phase O_2, which reacts with liquid-phase Fe, to form an oxide product of $Z_O = 0.5$, until all Fe is consumed.
2. The particle then ceases further intake of gas-phase O_2, and cools to the re-solidification temperature of Fe_3O_4.

The model based on the above mechanism is developed, and simulation results are compared to experimental measurements. Note that, the re-solidification process is not modeled in the current work, as there is no quantitatively accurate method to approximate the complex process, which likely involves some excess O_2 release from the particle, thermal expansion of trapped gas, and particle deformation due to gas ejection [28,35]. The model simulations are all stopped once the particle cools to the re-solidification temperature of Fe_3O_4.

3. Model for iron particle combustion

Due to the multi-phase nature of iron particle combustion, several models are required to capture its full combustion process. The model for solid-phase oxidation and formulations for the phase transition of iron/oxides are first presented. The detailed formulation for the liquid-phase iron particle combustion is subsequently described.

3.1. Solid-phase oxidation

Prior to the liquid-phase combustion of an iron particle, a solid-phase ignition process takes place. To capture this process, a solid-phase iron particle combustion model, based on oxidation kinetics

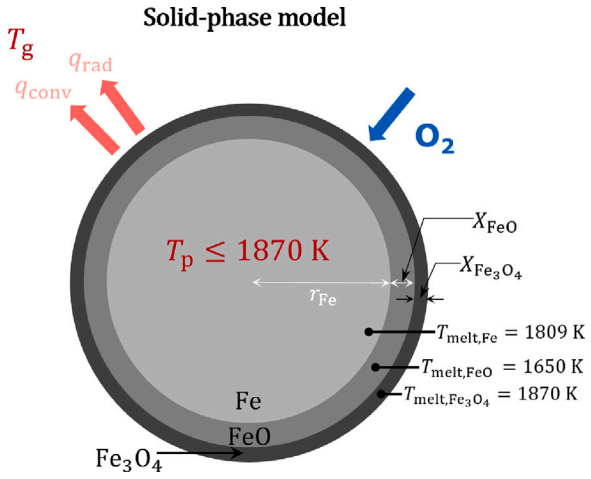

Fig. 2. Schematic of thermophysical model of a burning iron particle in a layer-by-layer structure in solid-phase and during solid-to-liquid phase transition.

calibrated to experimental data [8], developed by Mi et al. [14] is used, as illustrated in Fig. 2. As the current model aims to extend the ignition model, the formulation for the kinetic rate of oxide layer growth is modified to consider the shrinking-core effect:

$$\frac{dm_{FeO}}{dt} = \frac{4\pi\rho_{FeO,(s)} r_{FeO} r_{Fe}}{r_{FeO} - r_{Fe}} k_{0,FeO} \mathrm{Exp}\left[\frac{-T_{a,FeO}}{T_p}\right], \quad (1)$$

$$\frac{dm_{Fe_3rmO_4}}{dt} = \frac{4\pi\rho_{Fe_3O_4,(s)} r_{Fe_3O_4} r_{FeO}}{r_{Fe_3O_4} - r_{FeO}} k_{0,Fe_3O_4} \mathrm{Exp}\left[\frac{-T_{a,Fe_3O_4}}{T_p}\right]. \quad (2)$$

Here, $\rho_{FeO,(s)}$ and $\rho_{Fe_3O_4,(s)}$ denote the solid-phase densities of FeO and Fe_3O_4, respectively. The variables r_{Fe}, r_{FeO}, and $r_{Fe_3O_4}$ denote the Fe core radius, outer radius of the FeO spherical shell, and the outer radius of the Fe_3O_4 spherical shell (equivalent to the particle radius), respectively. The pre-exponential factor and activation temperature of FeO and Fe_3O_4 are empirically calibrated to experimental measurements of isothermal oxide layer growth, as described in [14]. The formation of Fe_2O_3 is neglected, as it only contributes to approximately 1% of the total oxide layer thickness, making the heat release associated with Fe_2O_3 formation negligible.

3.2. Solid-to-liquid phase transition of Fe, FeO, and Fe_3O_4

Between 1650 K and 1870 K, the phase transition of FeO (T_{melt} = 1650 K), Fe (T_{melt} = 1809 K), and Fe_3O_4 (T_{melt} = 1870 K) occur. In order to capture these processes, separate energy balance equations are solved in time. At temperatures other than the melting point of Fe, FeO, or Fe_3O_4, the change in total particle enthalpy is tracked to determine the increase in particle temperature. At the melting points, the change in particle enthalpy is used to track the increase in internal energy to overcome the respective latent heat of fusion:

$$\frac{dH_p}{dt} = -\frac{h_{O_2}}{W_{O_2}}\frac{dm_{O_2}}{dt} - A_p[h_p(T_p - T_g) + \epsilon\sigma(T_p^4 - T_g^4)] \text{ if } T_p \neq T_{melt,i}, \quad (3)$$

$$\frac{dH_{L,i}}{dt} = q_{FeO}\frac{dm_{FeO}}{dt} + q_{Fe_3O_4}\frac{dm_{Fe_3O_4}}{dt} - \frac{h_{O_2}}{W_{O_2}}\frac{dm_{O_2}}{dt} - A_p[h_p(T_p - T_g) + \epsilon\sigma(T_p^4 - T_g^4)] \text{ if } T_p = T_{melt,i}. \quad (4)$$

In Eq. (3), the variable H_p denotes the total enthalpy of the particle, which accounts for both enthalpy of formation and sensible enthalpy. The first term on the RHS accounts for the increase in particle enthalpy due to the incorporation of gaseous oxygen. The last two terms describe the convective and radiative heat loss, respectively. In Eq. (4), the variable $H_{L,i}$ tracks the sensible enthalpy of the particle at the phase-transition temperatures, and the heat release due to the formation of FeO and Fe_3O_4 are calculated explicitly via the first two terms on the RHS. The detailed formulation for these terms are described in [14]. The variable $H_{L,i}$ can be normalized by the latent heat of fusion and the mass of species i, $L_{f,i}$, to track the progress of the phase transition:

$$\frac{H_{L,i}}{L_{f,i}m_i} = \begin{cases} 1 & \text{if species } i \text{ in liquid phase,} \\ 0 \leq \frac{H_{L,i}}{L_{f,i}m_i} \leq 1 & \text{if during phase transition,} \\ 0 & \text{if species } i \text{ in solid phase.} \end{cases} \quad (5)$$

This normalized variable is used to track whether a given species is undergoing phase transition or not. Note that, during the solid-to-liquid phase transition of each species, oxidation reactions continue, and species masses evolve. When evaluating the particle temperature after a phase transition process with the total particle enthalpy, H_p, a temperature slightly different to the melting point is obtained, due to the change in species masses. To reconcile this, the total particle enthalpy is adjusted to a value that renders the correct particle temperature at the end of each phase transition process.

3.3. Extrapolation of iron oxidation kinetics to higher temperatures

It is of importance to elucidate the theoretical considerations around the extrapolation of the kinetic rate of iron oxidation to temperatures beyond what is experimentally verified (1523 K), to the melting point of FeO, Fe, and Fe_3O_4. Experimentally, the growth of the outermost oxide layer of Fe_2O_3 adapts to the gas-phase oxygen concentration, and allows the Fe cation and O anion activities at the Fe-FeO, FeO-Fe_3O_4, and Fe_3O_4-Fe_2O_3 interfaces to reach equilibrium [10,14]. As long as the Fe_2O_3 layer remains in solid-phase, its ability to equilibrate the internal interfacial activities should be preserved, therefore, the kinetic rate of FeO and Fe_3O_4 formation can be extrapolated to the melting point of Fe_2O_3 (1838 K). Additionally, this provides a theoretical basis for the assumption that absorbed oxygen is consumed to form FeO and Fe_3O_4 based on the oxidation activities determined by their individual kinetic rates, even during diffusion-controlled combustion. A simplification made in this model is the further extrapolation of the oxidation kinetics in the temperature range between the melting points of Fe_2O_3 and Fe_3O_4 (1838–1870 K), where the Fe cation and O anion activities at the phase interfaces may not necessarily be at a comparable equilibrium state. That being said, this assumption is only required if the oxidation rate is still kinetic-controlled past the melting point of Fe_2O_3, which is not the case for the range of simulations in this study [14].

3.4. Model formulation for a single molten droplet

In the current study, a zero-dimensional thermophysical model, based on the theoretical framework proposed by Soo et al. [36], is developed to describe the liquid-phase combustion of a single iron particle. This model considers a spherical droplet consisting of molten Fe (L1) and molten oxide (L2), assumed to be in a core and shell configuration with a shell of L2 phase around the core of L1 phase. This corresponds to the formation of oxide product to reach an oxidation stage of Z_O = 0.5 [6,31]. The assumption of L1 and L2 coexisting in the liquid-phase particle is based on the experimental evidence of a molten droplet with a mixed surface containing both L1 and L2 during the liquid-phase combustion of iron [26].

The model assumes the formation of liquid-phase FeO through reaction R1:

$$\text{R1}: \ \mathrm{Fe}(\ell) + \frac{1}{2}\mathrm{O}_{2(g)} \rightarrow \mathrm{FeO}(\ell). \quad (6)$$

Here, letters ℓ and g depict liquid- and gas-phase, respectively.

During the R1 oxidation stage, the dissociative evaporation of liquid-phase FeO is considered, through which gas-phase Fe, FeO, and FeO_2 are released, and is described by the following reaction R2 [6],

$$\text{R2}: \ \mathrm{FeO}(\ell) \leftrightarrow \mathrm{O(g)} + \mathrm{O_2(g)} + \mathrm{Fe(g)} + \mathrm{FeO(g)} + \mathrm{FeO_2(g)}. \quad (7)$$

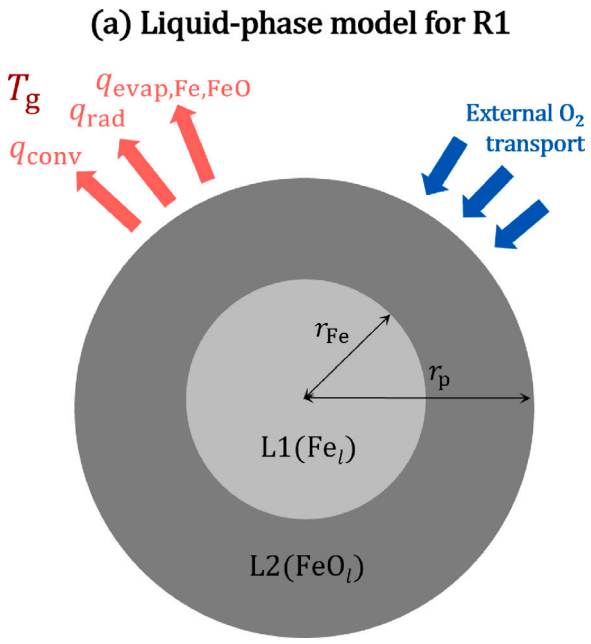

Fig. 3. Schematic of thermophysical model of a burning liquid-phase particle, illustrating the particle structure, mechanisms of heat transfer between the particle and gas, and O_2 intake for reaction R1.

Thermodynamic equilibrium calculations show that gas-phase Fe and FeO are the most significant dissociative evaporation products from liquid-phase FeO, as illustrated in Fig. 4. Hence, the gas-phase diffusion of Fe and FeO away from the particle are considered in the gas-transport model. Note that the direct evaporation of liquid-phase Fe is not considered, since the model assumes only the L2 phase to be in contact with the gas-phase environment, as depicted in Fig. 3.

Note that since FeO is the most dominant product of iron oxidation in solid-phase, the particle does not contain a significant amount of Fe_3O_4 at the onset of liquid-phase combustion. Moreover, the equilibrium vapor pressure of liquid-phase Fe_3O_4 is more than an order of magnitude lower than that of liquid-phase FeO [6]. The evaporation of Fe_3O_4 is, therefore, neglected in this study.

While there is likely a complex interaction of gas-phase oxidation reactions governed by gas-phase kinetics [37–40], a simplifying assumption is made in the model, such that gas-phase Fe and FeO oxidize and condense into Fe_2O_3 by instantaneously consuming inward-transported O_2 to the particle via the following reactions R3 and R4:

$$\mathrm{R3}: 2\mathrm{Fe(g)} + \frac{3}{2}\mathrm{O_{2(g)}} \rightarrow \mathrm{Fe_2O_3(s)}. \tag{8}$$

$$\mathrm{R4}: 2\mathrm{FeO(g)} + \frac{1}{2}\mathrm{O_{2(g)}} \rightarrow \mathrm{Fe_2O_3(s)}. \tag{9}$$

The letter "s" denotes solid-phase. By consuming inward-transported O_2, reactions R3 and R4 reduce the overall rate of O_2 transport to the particle, inhibiting the rate of heat release from the particle. While the dissociation of gas-phase FeO into gas-phase Fe and O_2 can also occur at elevated gas temperatures, this process is neglected since these products will go through the reverse reaction to re-form gas-phase FeO, and this dissociation/reformation process bears no effect on the overall thermodynamics of the system.

3.4.1. Mass and energy balance equations

The mass and energy balance equations described here are solved over time to track the mass of Fe and FeO inside the particle, and the total enthalpy of the particle. The formation of Fe_3O_4 in liquid-phase is not considered due to reasons considered in Section 2, and the formation of Fe_2O_3 in liquid-phase is not considered, as it is thermodynamically unstable past its melting point. We introduce the following expression for the total rate at which the particle consumes O_2 gas:

$$\frac{\mathrm{d}m_{\mathrm{O_2}}}{\mathrm{d}t} = -(\dot{m}_{\mathrm{O_2}} - \nu_{\mathrm{O_2}/Fe,(g)}\dot{m}_{\mathrm{Fe}} - \nu_{\mathrm{O_2}/FeO,(g)}\dot{m}_{\mathrm{FeO}}). \tag{10}$$

Here, $\dot{m}_{\mathrm{O_2}}$, $\dot{m}_{\mathrm{Fe}}$, and $\dot{m}_{\mathrm{FeO}}$ each denote the external mass transport rate of gas-phase O_2, Fe, and FeO. The variables $\nu_{\mathrm{O_2}/Fe,(g)}$ and $\nu_{\mathrm{O_2}/FeO,(g)}$ denote the stoichiometric mass ratios for the gas-phase reactions R3 and R4. The rate of O_2 reaching the particle is reduced by the rate at which gas-phase Fe and FeO consume inward-diffused O_2. The mass balance equations for liquid-phase Fe and FeO in the particle during the R1 oxidation step of the liquid-phase combustion are then written as follows:

$$\frac{\mathrm{d}m_{\mathrm{Fe}}}{\mathrm{d}t} = \nu_{\mathrm{Fe}/\mathrm{O_2},(\ell)}\frac{\mathrm{d}m_{\mathrm{O_2}}}{\mathrm{d}t}, \tag{11}$$

$$\frac{\mathrm{d}m_{\mathrm{FeO}}}{\mathrm{d}t} = -\nu_{\mathrm{FeO}/\mathrm{O_2},(\ell)}\frac{\mathrm{d}m_{\mathrm{O_2}}}{\mathrm{d}t} - \dot{m}_{\mathrm{FeO,evap}}. \tag{12}$$

The overall gas-phase O_2 consumption rate is multiplied by the stoichiometric mass ratios for the liquid-phase reaction R1, $\nu_{\mathrm{Fe}/\mathrm{O_2},(\ell)}$ and $\nu_{\mathrm{FeO}/\mathrm{O_2},(\ell)}$, to give the consumption and formation rate of liquid-phase Fe and FeO, respectively. The evaporative mass loss of liquid-phase FeO, $\dot{m}_{\mathrm{FeO,evap}}$, is defined as the sum of the contributions from the release of gas-phase Fe and FeO:

$$\dot{m}_{\mathrm{FeO,evap}} = \dot{m}_{\mathrm{FeO}} + \frac{M_{\mathrm{FeO}}}{M_{\mathrm{Fe}}}\dot{m}_{\mathrm{Fe}}. \tag{13}$$

The total enthalpy of the particle H_{p} is calculated as the sum of the enthalpy of each condensed-phase species,

$$H_{\mathrm{p}} = \sum_{j}^{N_{\mathrm{s}}} \frac{m_j h_j(T_{\mathrm{p}})}{M_j}, \tag{14}$$

where N_{s} is the total number of species, m_j is the mass of the jth species, h_j is the molar enthalpy of the jth species as a function of particle temperature T_{p} calculated using the NASA 7-coefficient polynomial parametrization [41], and M_j is the molecular weight of the jth species. With the particle enthalpy H_{p} and species masses m_j known, the particle temperature can be determined via a root-finding iterative scheme.

The particle enthalpy evolves according to the rate of addition of the enthalpy due to the incorporated oxygen, heat loss rate due to the heat exchange with the surrounding gas via convection and radiation, and heat loss rate due to the evaporation of condensed-phase iron and iron oxide species. The following equation is solved in time to track the evolution of particle enthalpy:

$$\frac{\mathrm{d}H_{\mathrm{p}}}{\mathrm{d}t} = -\frac{h_{\mathrm{O_2}}}{M_{\mathrm{O_2}}}\frac{\mathrm{d}m_{\mathrm{O_2}}}{\mathrm{d}t} - 2\pi \mathrm{Nu_{St}} r_{\mathrm{p}} \lambda (T_{\mathrm{p}} - T_{\mathrm{g}}) - A_{\mathrm{p}}\epsilon\sigma(T_{\mathrm{p}}^4 - T_{\mathrm{g}}^4) - \frac{h_{\mathrm{Fe}}}{M_{\mathrm{Fe}}}\dot{m}_{\mathrm{Fe}} - \frac{h_{\mathrm{FeO}}}{M_{\mathrm{FeO}}}\dot{m}_{\mathrm{FeO}}. \tag{15}$$

Note that explicit formulations of the heat release associated with the formation of oxide products are not included in Eq. (15), since the computation of the total particle enthalpy in Eq. (14) takes into account the heat of formation of species. The first term on the right-hand side of Eq. (15) describes the addition of the enthalpy of oxygen consumed by the particle. The total molar enthalpy of gas-phase O_2, Fe, and FeO are represented by $h_{\mathrm{O_2}}$, h_{Fe}, and h_{FeO}, and are calculated using polynomials given by the NASA database [41]. The second term describes the convective heat loss rate as a function of the Stefan-corrected Nusselt number, $\mathrm{Nu_{St}}$ [42], considering the slip velocity between the particle and the gas. The particle is assumed to be at the terminal velocity [43] evaluated at boundary-layer-averaged gas conditions. The variable λ denotes the gas-phase thermal conductivity, calculated using the Cantera toolbox. Boundary-layer-averaged values

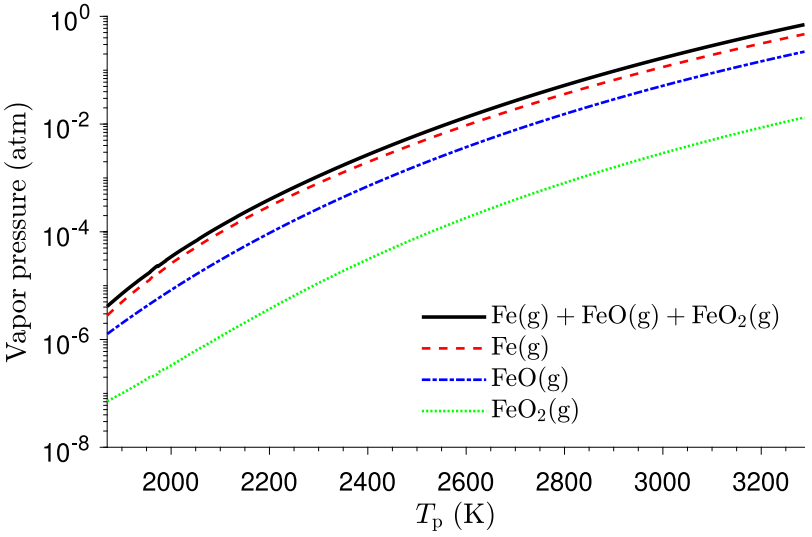

Fig. 4. Vapor pressure of Fe-containing species evaporating from liquid-phase FeO determined via thermodynamic equilibrium calculations on Cantera, for the temperature range 1870–3280 K at 1 atm.

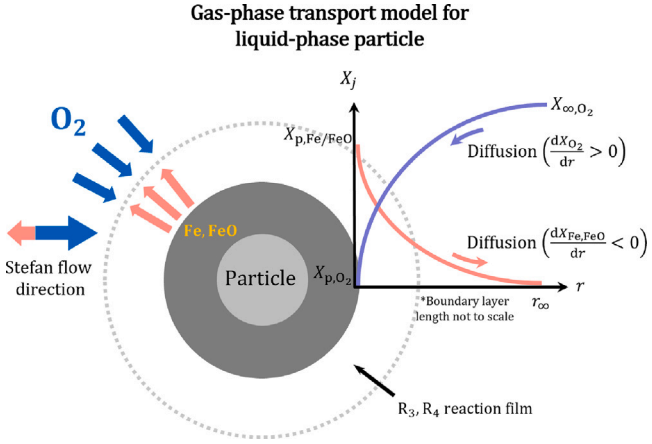

Fig. 5. Schematic describing gas-phase transport through the boundary layer in the vicinity of the particle surface, where O_2 is transported by diffusion and Stefan flow to the particle surface, and Fe and FeO diffuse away from the particle surface due to evaporation.

are used for the gas temperature and molar composition, calculated via the 1/2 averaging rule [42]:

$$T_{g,f} = \frac{1}{2}(T_g + T_p), \tag{16}$$

$$X_{i,f} = \frac{1}{2}(X_{i,g} + X_{i,p}). \tag{17}$$

The symbols ϵ and σ in the radiative heat transfer term denote the emissivity of the particle and the Stefan–Boltzmann constant, respectively. Here, the emissivity of the molten droplet is taken as 0.7 [26], as the outer surface of the molten droplet will consist of L2 phase. The last two terms on the right-hand side of Eq. (15) describe the heat loss due to the evaporation of Fe and FeO. Since the heat release associated with the gas-phase oxidation reactions are insignificant compared to the heat capacity of the surrounding bulk gas, the enthalpy of gas-phase reactions are neglected.

3.4.2. Gas-phase transport

At the onset of external-O_2-transport-limited combustion, the lack of O_2 at the particle surface generates a low pressure region, driving a Stefan flow from the bulk gas toward the particle surface. While Fe and FeO may evaporate from the particle surface, as experimental measurements show that iron particles only reach a peak temperature well below the boiling point of Fe, the mass flux of O_2 toward the particle will likely be much greater than the mass flux of gas-phase Fe and FeO away from the particle as depicted in Fig. 5. Therefore, the direction of Stefan flow is likely always toward the particle [44]. In the current model, an external mass transport rate considering Stefan flow and diffusion is used for O_2, while the gas-phase Fe and FeO is assumed to be transported by diffusion only.

The partial pressures of gas-phase O_2, Fe, and FeO at the surface are determined via their vapor pressures from thermodynamic equilibrium between species described in R2 (Eq. (7)). The partial pressure of the inert gas species (N_2 in this study) is calculated such that the partial pressures of evaporating species and N_2 add up to 1 atm. The mole fraction of each gas-phase species at the surface are then evaluated via Dalton's law. Lennard-Jones (LJ) potential parameters, (σ_j, ϵ_j), for Fe and FeO are taken from [45]. The external mass transport rate of O_2 is:

$$\dot{m}_{O_2} = 2\pi \mathrm{Sh}_{St} r_p \rho_{O_2} \mathcal{D}_{O_2} (X_{O_2,g} - X_{O_2,p}). \tag{18}$$

Here, a Stefan-corrected Sherwood number correlation applicable to iron particle combustion is used [42]. The transport rate is hindered by the presence of O_2 at the particle surface resulting from the dissociative evaporation reaction in Eq. (7). The external mass transport rate of gas-phase Fe and FeO are of the following form:

$$\dot{m}_j = 2\pi \mathrm{Sh} r_p \rho_j \mathcal{D}_j X_{j,p}. \tag{19}$$

The variables D_{O_2} and D_j each denote the mass diffusivity of O_2 and evaporating species, and are calculated using the Cantera toolbox, evaluated at a boundary-layer-averaged state via the 1/2 averaging rule. The density of each gas, ρ_{O_2} and ρ_j, follow the form [42],

$$\rho_i = \frac{p_0}{\mathcal{R}_{g,i} T_{g,f}}, \tag{20}$$

where p_0 is the total pressure in the gas, $\mathcal{R}_{g,i}$ is the specific gas constant for species i, and $T_{g,f}$ is the boundary-layer-averaged gas temperature. The values and correlations used for key liquid- and vapor-phase properties are summarized in Table 1:

4. Sample results compared to experimental measurements

Sample results of the model simulation are presented in comparison to two independent sources of experimental results on single particle

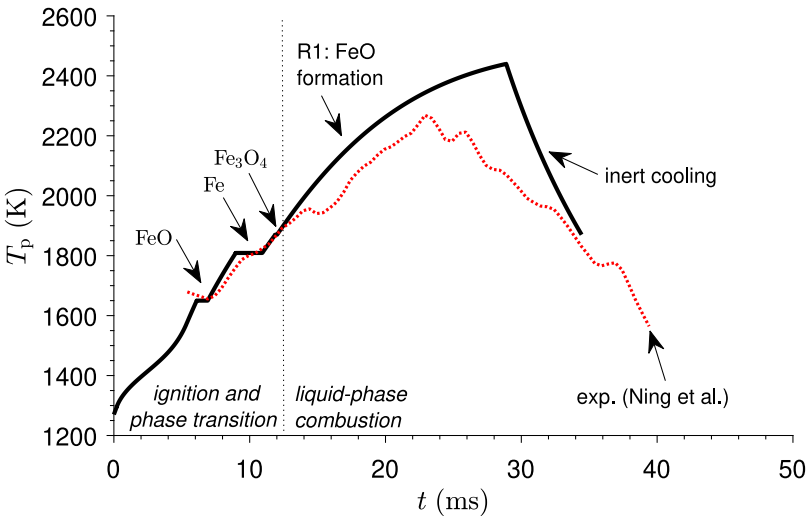

Fig. 6. Time history of particle temperature predicted by the model considering only liquid-phase FeO formation (black solid), compared to a typical smoothened experimental temperature profile of a laser-ignited particle by Ning et al. [6] (red dotted). Initial conditions: $d_{p,0} = 54\,\mu m$ $T_g = 300$ K, $X_{O_2} : X_{N_2} = 0.21 : 0.79$. (For interpretation of the references to color in this figure legend, the reader is referred to the web version of this article.)

Table 1
Liquid- and vapor-phase properties of Fe and FeO.

Property	Name	Value	Unit
$\rho_{Fe,\ell}$	Liquid-phase density of Fe	$8523–8.358 \times 10^{-4} T$ [46]	kg m^{-3}
$\rho_{FeO,\ell}$	Liquid-phase density of FeO	4350 [47]	kg m^{-3}
$L_{Fe,f}$	Latent heat of fusion of Fe	2.090×10^5	J kg^{-1}
$L_{FeO,f}$	Latent heat of fusion of FeO	4.251×10^5	J kg^{-1}
ϵ_{Fe}, ϵ_{FeO}	Potential well depth	3000	K
σ_{Fe}, σ_{FeO}	Lennard-Jones diameter	4.3	Å

combustion [6,7]. The model is first compared to a typical temperature profile of a laser-ignited iron particle burning in air at 300 K. The model is subsequently compared to temperature profiles of particles burning in a drop tube furnace in gas of varying oxygen concentrations at 1350 K. For all simulations, the initial oxide layer thickness to particle size ratio is set to a value of 10^{-3}, to ensure that the initial temperature of the particle required for ignition is minimized [14].

4.1. Combustion in ambient temperature air

To compare the current model results to experimental results on the combustion of laser-ignited single iron particles by Ning et al. [6], the initial particle diameter is set to $d_{p,0} = 54\,\mu m$, with ambient gas conditions of $T_g = 300$ K and 21% O_2, 79% N_2 by volume. The initial particle temperature is set to $T_p = 1270$ K to ensure a thermal runaway. Note that this value is higher than the ignition limit predicted by Mi et al. [14], as ambient gas temperatures are assigned.

The results are plotted in Fig. 6. To compare the combustion time and peak temperature predicted by the model to the experimental temperature profile, the temperature curves are shifted such that they coincide at the melting point of FeO. The particle first undergoes solid-phase ignition, where the combustion rate is initially limited by solid-phase oxidation kinetics. As the particle temperature increases and the combustion transitions into an external-O_2-transport-limited regime, the phase change of FeO, Fe, and Fe_3O_4 are observed sequentially, represented by the flat temperature profiles at 1650 K, 1809 K, and 1870 K, respectively. The particle continues to burn in the external-O_2-transport-limited regime until all Fe has been consumed at around 28.9 ms, reaching a temperature of about 2440 K. This slightly overpredicts the peak temperature of the experimental curve of 2268 K, occurring at around 22.9 ms. The particle temperature begins to drop when $Z_O = 0.5$ is reached, via heat loss through evaporation of Fe and FeO, convection, and radiation. The simulation is stopped once the particle temperature reaches the re-solidification point of Fe_3O_4 (1870 K). The model does not appear to capture the rate of cooling seen in the experiment.

Fig. 7 (*upper*) plots the rates of heat release, heat losses, and heat loss due to evaporation over time. The heat loss rate is split up into the contributions of convective, radiative, and evaporative heat loss. The heat loss rate due to evaporation is the sum of contributions from the evaporation of Fe and FeO, both as described in Eq. (15). The rate of heat release associated with solid-phase FeO and Fe_3O_4 are described by Eqs. (1) and (2), with specific energy release values as detailed in [14]. For the liquid-phase combustion, the rate of heat release is approximated as the sum of the enthalpy of formation of liquid-phase FeO and the addition of enthalpy due to the incorporation of gaseous O_2 to the particle:

$$\dot{Q}_{release} = q_{FeO,\ell}\left(-\nu_{FeO/O_2,(\ell)}\frac{dm_{O_2}}{dt}\right) - \frac{h_{O_2}}{M_{O_2}}\frac{dm_{O_2}}{dt}. \tag{21}$$

The variable $\nu_{FeO/O_2,(\ell)}$ denotes the stoichiometric mass ratio for the condensed-phase reaction R1, and the term $\frac{dm_{O_2}}{dt}$ is the consumption rate of O_2 gas by the particle described in Eq. (18). The variable $q_{FeO,\ell}$ denotes the specific energy release associated with the formation of liquid-phase FeO, and can be estimated as follows:

$$q_{FeO,\ell} = -\Delta H^{\circ}_{f,FeO(\ell)}/M_{FeO}. \tag{22}$$

The standard heat of formation of liquid-phase FeO is taken from [48].

The heat release rate curve in Fig. 7 (*upper*) elucidates the various combustion regimes an iron particle undergoes during its combustion process. During solid-phase ignition, the high initial particle temperature facilitates an initially O_2 transport-controlled combustion, which quickly transitions into a kinetic-controlled combustion. The rapid growth of the oxide layers initially inhibits the rate of oxide product formation (~2 ms), until the exponential dependence on particle temperature of the Arrhenius term begins to dominate (2 ~ 5 ms). The subsequent flat heat release rate indicates a transition to a external-O_2-transport-limited combustion regime, resembling double transition behavior [14]. The discontinuous drop in heat release rate observed at around 7 ms is attributed to the lower specific energy release of FeO in liquid-phase compared to solid-phase due to the latent heat of fusion. The heat release rate then continues to increase until all Fe is consumed. Note that the heat loss rate increases more rapidly than the heat release rate, as the convective rate of heat loss is linear

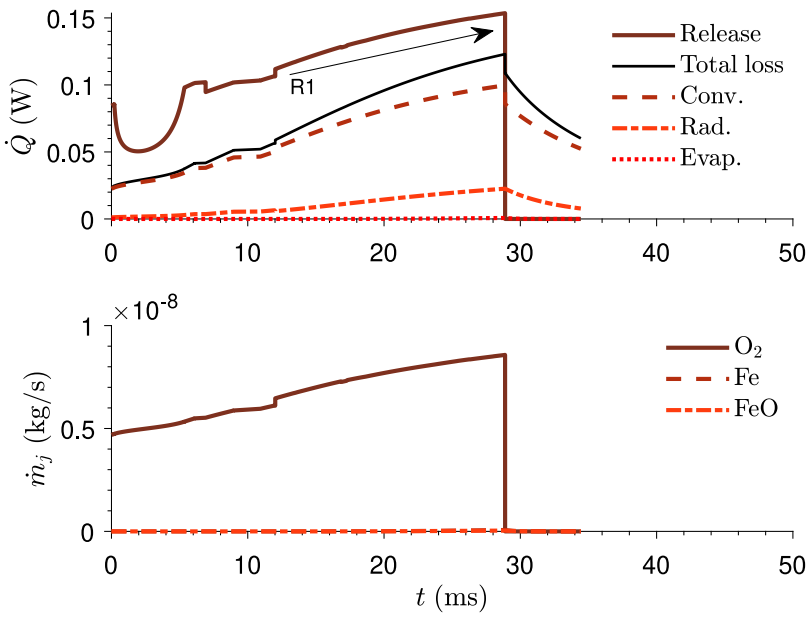

Fig. 7. The time-evolution of (*upper*) rate of heat release (solid), total rate of heat loss (thin solid), rate of convective heat loss (dashed), rate of radiative heat loss (dash-dotted), rate of heat loss due to evaporation (dotted), and (*lower*) mass transport rate of gas-phase O_2 to the particle surface (solid), gas-phase Fe away from the particle surface (dashed), and gas-phase FeO away from the particle surface (dash-dotted). Initial conditions: $d_{p,0} = 54\,\mu m$, $T_g = 300$ K, $X_{O_2} : X_{N_2} = 0.21 : 0.79$.

in the particle/gas temperature gradient, while the heat release rate, dependent upon the external O_2 transport rate, is weakly dependent on temperature. The increase in particle enthalpy therefore slows down, reconciling the increasingly flattening increase in particle temperature predicted by the model. It is also important to note that the contribution of radiative heat loss is much less significant compared to the convective heat loss, and that the heat loss due to evaporation plays a negligible role in the combustion dynamics for a single particle burning at ambient gas temperature in 21% O_2. The particle then cools to its re-solidification point through convective, radiative, and evaporative heat loss.

Fig. 7 (*lower*) plots the rates of mass transport of gas-phase O_2, Fe, and FeO. The rate of gas-phase transport of O_2 slowly increases as the particle heats up in the liquid-phase combustion process, as the external diffusion rate is weakly dependent on the particle temperature. The rates of gas-phase transport of Fe and FeO are more sensitive to temperature, as the vapor pressures of the evaporating species are exponentially dependent on temperature. For the case of a 54 μm particle burning in ambient air conditions, the evaporation is minimal.

4.2. Combustion in high temperature environments

The current model is also compared to the particle temperature profiles of drop-tube furnace experiments in high temperature gas obtained by Panahi et al. [7]. Experiments were performed with particles of initial diameter ranging between 38 and 45 μm and between 45 and 53 μm, with drop-tube walls set to a temperature of $T_g = 1350$ K, which simulates the conditions which particles experience upon entering a real combustor. The range of experimentally measured particle temperatures are plotted as a band of temperature trajectories, for model comparison. The experimental temperature measurement curves are shifted forward in time such that the lowest averaged experimental temperature data point collapses with the model result, to facilitate comparison of the bulk of the liquid-phase combustion period. The same initial particle temperature of $T_p = 1270$ K is prescribed in all simulations.

4.2.1. Combustion in high temperature air

Fig. 8 presents the particle temperature profiles predicted by the current model. In Fig. 8, the particle temperature sharply increases and reaches its peak of 2825 K at around 13.1 ms, compared to 2478 K at 12 ms in the averaged experimental measurement. A plateau-like behavior in particle temperature is observed in the model simulation near the peak temperature. The particle then undergoes cooling to the re-solidification temperature of Fe_3O_4. The cooling rate of the particle is, again, overpredicted in the model, since the predicted rate of temperature decrease at around 16 ms, where the model-predicted temperature and experimental temperature measurement coincide, is much faster than in the experimental measurement. These results show that a model considering external-O_2-transport-limited combustion considering only liquid-phase FeO formation during the liquid-phase combustion significantly overpredicts the increase in particle temperature, as well as the cooling rate.

Fig. 9 is qualitatively similar to Fig. 7, but is plotted for the high gas temperature simulation ($T_g = 1350$ K) with an initial particle diameter of 42 μm. The rate of heat release in Fig. 9 (*upper*) exhibits a double-transition behavior [14], where the combustion begins at an external-O_2-transport-limited rate, followed by a transition to kinetically-controlled combustion, and then finally a transition back into external-O_2-transport-limited combustion. While the heat release rates in solid-phase and during phase transition are comparable to the case with combustion in ambient gas conditions, the heat release rate drops shortly after transitioning into liquid-phase combustion (annotated as A1), contrary to the monotonic increase in heat release rate during FeO formation in the ambient gas case. This is due to the increased vapor pressure of gas-phase products formed via the dissociative evaporation of the L2 oxide phase, facilitated by the high particle and gas temperatures. This leads to an increase in the rate of Fe and FeO evaporation, which limit the mass transport rate of O_2 to the particle surface due to the initial consumption of inward O_2 by outward gas-phase Fe and FeO through reactions R3 and R4. The increased production of gas-phase O_2 at the particle surface due to the dissociative evaporation of liquid-phase FeO also reduces the concentration gradient of O_2 between the bulk gas and particle surface, thereby reducing the mass transport rate of O_2 as well. The increased evaporation rates and increasing particle temperature lead

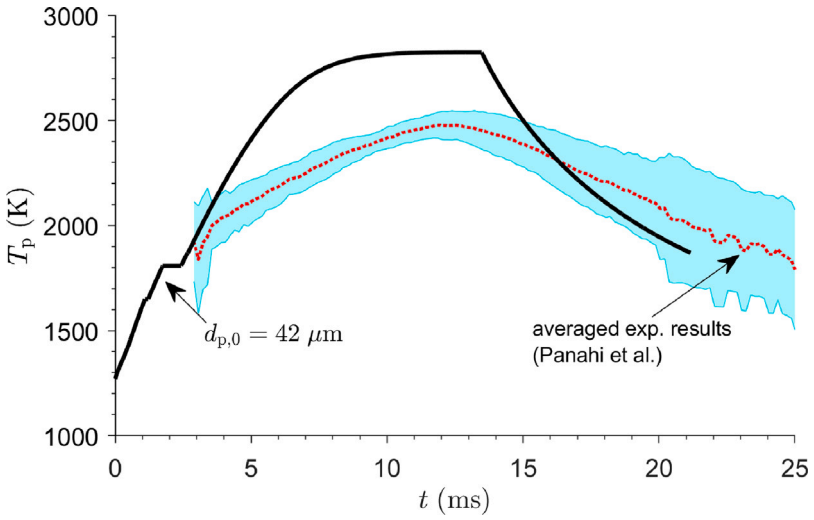

Fig. 8. Time history of particle temperature predicted by the model considering only liquid-phase FeO formation (black solid) for $d_{p,0}$ = 42 μm, compared to an averaged experimental particle temperature profile (red dotted), and one standard deviation above and below the average particle temperature (light blue band). Gas conditions: T_g = 1350 K, $X_{O_2} : X_{N_2} = 0.21 : 0.79$. (For interpretation of the references to color in this figure legend, the reader is referred to the web version of this article.)

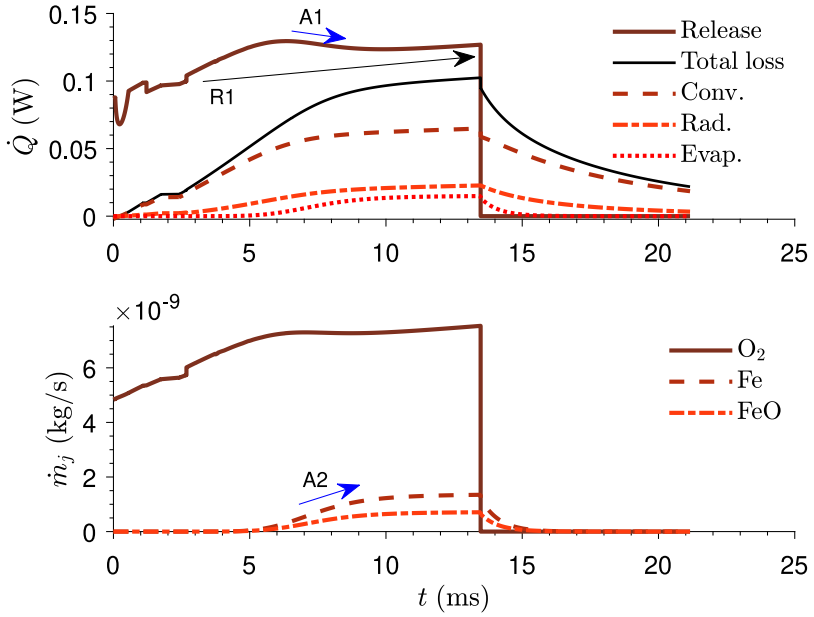

Fig. 9. The time-evolution of (*upper*) rate of heat release (solid), total rate of heat loss (thin solid), rate of convective heat loss (dashed), rate of radiative heat loss (dash-dotted), rate of heat loss due to evaporation (dotted), and (*lower*) mass transport rate of gas-phase O_2 to the particle surface (solid), gas-phase Fe away from the particle surface (dashed), and gas-phase FeO away from the particle surface (dash-dotted). Initial conditions: $d_{p,0}$ = 42 μm, T_g = 1350 K, $X_{O_2} : X_{N_2} = 0.21 : 0.79$.

to a heightened rate of heat loss due to evaporation, convection, and radiation.

It can also be observed that, for a particle burning in high temperature gas, and, therefore, with high evaporation rates, this model predicts a peak particle temperature that occurs during the oxidation stage to Z_O = 0.5, dictated by the rates of heat release, heat loss by convection and radiation, and heat loss due to evaporation. The particle naturally reaches a sufficiently high temperature that facilitates a rate of total heat loss, which counteracts the rate of heat release limited by the rate of O_2 transport to the particle surface. Fig. 9 shows that the rate of heat release and total heat loss do not exactly equilibrate. However, the increase in particle enthalpy is slow, and the particle heat capacity increases since liquid-phase FeO has a higher heat capacity than that of liquid-phase Fe. The model, therefore, predicts a very slow increase in particle temperature. It may be noted that a similar plateau in temperature was observed in experiments conducted by Dreizin et al. [49] using steel droplets of 180 μm in diameter. It is possible that the burning droplet reached a similar state where the rates of heat release and heat loss equilibrate, such that the particle continues to burn at a steady temperature.

4.2.2. Combustion in higher oxygen concentrations

The current models are compared to averaged experimental measurements of particle temperature in a 50% O_2, 50% N_2 environment in Fig. 10(a). The model overpredicts the experimental measurements, predicting a peak temperature of around 3160 K at 5 ms, compared to the experimental measurement of 2814 ± 27 K.

To compare the current model results to experimental results on combustion in high temperature pure O_2 conditions, the gas composition in the model is set to 99% O_2 and 1% N_2 by volume. This approximately models the maximum diffusion rate of O_2, while ensuring proper computation of the binary diffusion coefficients of O_2 in

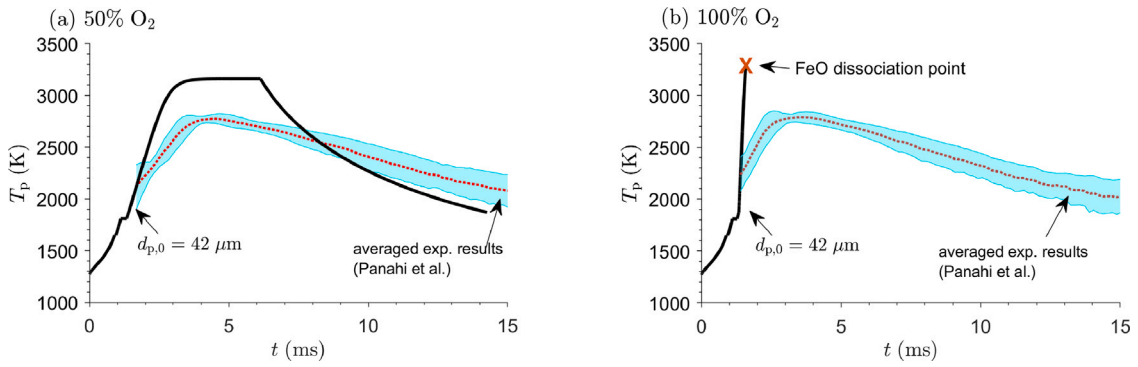

Fig. 10. Time histories of particle temperature predicted by the model considering only FeO formation in liquid-phase (black solid), compared to averaged experimental temperature profiles (red dotted) for a particle burning in (a) 50% O_2, 50% N_2 and (b) pure O_2, with the solid light blue band representing one standard deviation above and below the average particle temperatures. Initial conditions: $d_{p,0} = 42\,\mu$m, $T_g = 1350$ K, with molar fractions (a) $X_{O_2} : X_{N_2} = 0.50 : 0.50$ and (b) $X_{O_2} : X_{N_2} = 0.99 : 0.01$. (For interpretation of the references to color in this figure legend, the reader is referred to the web version of this article.)

gas-transport calculations. The simulation result shown in Fig. 10(b) is cut off at 3280 K, since the thermochemical equilibrium calculations fail to predict the vapor pressure of gas-phase species evaporating from liquid-phase FeO past this point, and the experiments conducted in [7] do not observe such a high temperature, nor any rapid vaporization of the particle. The model result sharply overpredicts the experimental measurement of 2835 ± 34 K.

5. Analysis

5.1. Comparison with experimental measurement

The simulated particle temperature for combustion in ambient air (Fig. 6) slightly overpredicts the typical experimental temperature profile. In comparison to experimental measurements in high temperature O_2/N_2 mixtures (Figs. 8, 10), the agreement between model and experiment is inadequate, and is increasingly worse for combustion in higher oxygen concentrations. In terms of qualitative observations, while the model predicts a plateau-like behavior at the peak temperature for combustion in high temperature gas, no plateau in peak temperature was observed in the experiments by Panahi et al. [7]. In general, the model considering external-O_2-transport-limited combustion in liquid-phase consistently overpredicted the peak particle temperature in comparison to experimental measurement.

It is important to note that only the oxidation to an intermediate oxidation stage, $Z_O = 0.5$, was considered in this study, and the further oxidation to the molar ratio of stoichiometric Fe_3O_4 was neglected. Thus, the considered contribution to heat release within the particle is likely to be underestimated. Yet, the model simulation consistently overpredicts the peak particle temperature. This result may indicate that, perhaps, some internal mechanism becomes rate-limiting during liquid-phase combustion and, therefore, the assumption of external-O_2-transport-limited combustion, during liquid-phase iron particle combustion, may be flawed.

The model predictions also depart after reaching $Z_O = 0.5$ (full conversion of liquid-phase Fe to "liquid-phase FeO"). The current model considers cooling to the re-solidification temperature of Fe_3O_4 via Fe and FeO evaporation, convective heat loss, and radiative heat loss. This appears to overpredict the cooling rate, as cooling curves predicted by this model have a steeper gradient than the experimental measurement and/or diverge under the experimental cooling curve, as seen in Figs. 6, 8, and 10. The possibility of a cloud of nano-oxides forming a protective shell shielding the particle from heat loss to the bulk gas is unlikely, as Fig. 3 from Panahi et al. [7] indicates that, once the peak particle temperature has been reached at around 18–20 ms, the dark plume of vapor-phase products appear to be convected away from the particle, exposing the particle to the bulk gas surroundings.

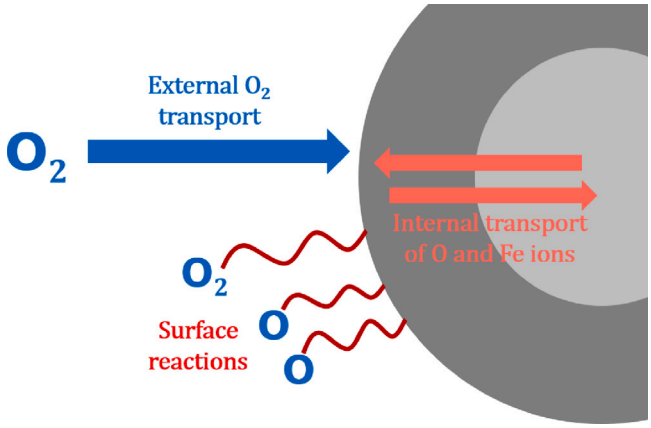

Fig. 11. Potential rate-limiting mechanisms of liquid-phase iron particle combustion.

5.2. Rate-limiting mechanisms of iron particle combustion

The model prediction based on liquid-phase FeO formation at the external-O_2-transport-limited rate consistently overpredicts the experimental measurement of particle temperature during the particle heating phase, as shown in Figs. 6, 8, and 10. Moreover, the model considering inert cooling overpredicted the cooling rate. It is possible that some oxidation and heat release is occurring during the cooling phase, as the cooling curves in the measurements by Ning et al. [6] and Panahi et al. [7] resemble relatively straight lines, while a pure-cooling curve should have a steep gradient at the peak, gradually tapering off to a plateau near the surrounding gas temperature. These findings motivate the exploration of other possible mechanisms that may be rate-limiting during the liquid-phase combustion of a single iron particle (see Fig. 11).

The heterogeneous nature of iron particle combustion gives rise to multiple sequential mechanisms that precede the formation of oxide products. Oxygen is supplied from the external gas-phase environment via diffusion and Stefan flow, which interacts with the particle surface via physical and chemical adsorption processes. The reactive O and Fe ions must then be transported within the particle, and finally a chemical reaction can take place. The current model assumes the external O_2 transport to be rate-limiting during liquid-phase combustion, and consistently overpredicts the peak particle temperature compared to experimental measurement. A recent work by Thijs et al. [50] performed molecular dynamics simulations to determine the accommodation coefficient at the particle surface for a range of oxygen ion mole fractions in the oxide product. An iron particle combustion model, considering

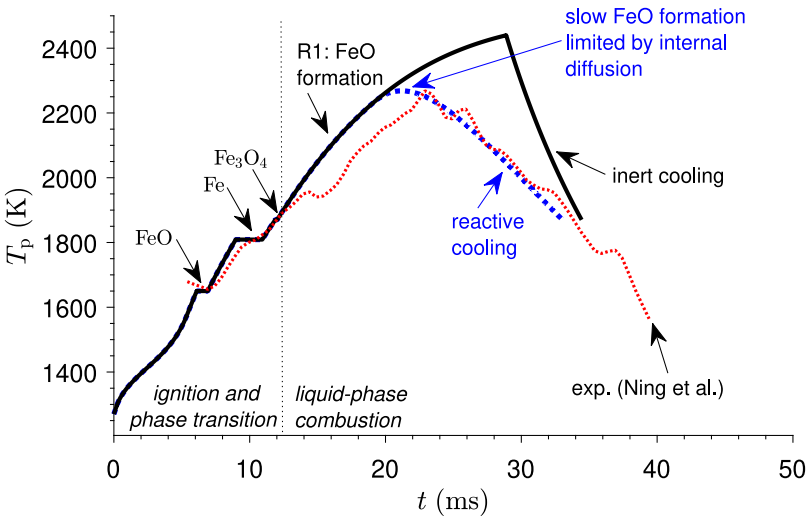

Fig. 12. Time history of particle temperature predicted by model assuming O_2-transport-limited liquid-phase FeO formation (black solid) and the heuristic model considering internal diffusion limiting the rate of oxidation (blue dashed), compared to a typical smoothened experimental temperature profile of a laser-ignited particle by Ning et al. [6] (red dotted). Initial conditions: $d_{p,0} = 54\,\mu m$, $T_g = 300$ K, $X_{O_2} : X_{N_2} = 0.21 : 0.79$. (For interpretation of the references to color in this figure legend, the reader is referred to the web version of this article.)

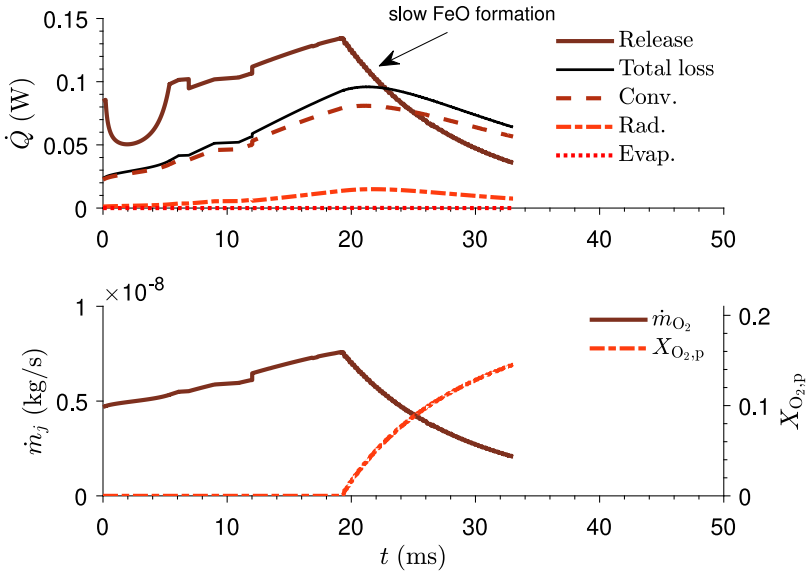

Fig. 13. The time-evolution of rate of heat release (solid), total rate of heat loss (thin solid), rate of convective heat loss (dashed), rate of radiative heat loss (dash-dotted) (*upper*), and mass transport rate of gas-phase O_2 to the particle surface (dash-dotted) and surface mole fraction of O_2 during the internal-diffusion-limited liquid-phase FeO formation (dashed) (*lower*) for the heuristic model considering internal kinetics. Initial conditions: $d_{p,0}$ =54 μm, $T_g = 300$ K, $X_{O_2} : X_{N_2} = 0.21 : 0.79$.

surface reactions with a changing accommodation coefficient hindering the rate of heat release, was shown to achieve better agreement with experimental measurement. However, this model still overpredicts the peak particle temperature and, therefore, the consideration of surface reactions alone likely does not fully resolve the discrepancy between model results and experimental measurement. From this, one can postulate that the internal transport of O and Fe ions may also become a rate-determining step in the liquid-phase combustion of iron particles.

A complete model for single iron particle combustion may require resolving all aforementioned processes, including the boundary layer between the particle and the gas, surface reactions at the particle-gas interface, as well as the internal boundary layer within the particle, considering the transport of reactive O and Fe ions. While this is a substantial modeling effort outside the scope of the current work, a first approach to modeling internal-diffusion-limited combustion is herein presented. A simplified analysis is provided through a heuristic model, to explore the effect of considering the effects of such a rate-limiting mechanism on the combustion behavior of a single iron particle.

The mathematical formulation for the rate of internal diffusion of reactive ions through a spherical shell is analogous to the solid-phase oxidation rate presented in Eqs. (1) and (2):

$$\frac{dm_{FeO}}{dt} = \frac{4\pi\rho_{FeO,\ell} r_{FeO} r_{Fe}}{X_{FeO}} k_{0,diff.,FeO,\ell} \mathrm{Exp}\left[-\frac{T_{a,FeO,\ell}}{T_p}\right]. \quad (23)$$

The activation temperature in the Arrhenius term is defined as $T_{a,FeO,\ell} = E_{a,FeO,\ell}/\mathcal{R}$, and corresponds to the activation temperature related to the internal diffusion of reactive ions through a liquid-phase FeO layer. The variable X_{FeO} is the liquid-phase FeO layer thickness calculated as $X_{FeO} = r_p - r_{Fe}$. In Eq. (23), the r_{Fe} term asymptotically decreases to zero as the liquid-phase Fe in the particle is consumed, and the X_{FeO} term linearly decreases the oxidation rate as the liquid-phase FeO layer thickens. These two terms act against the exponential increase

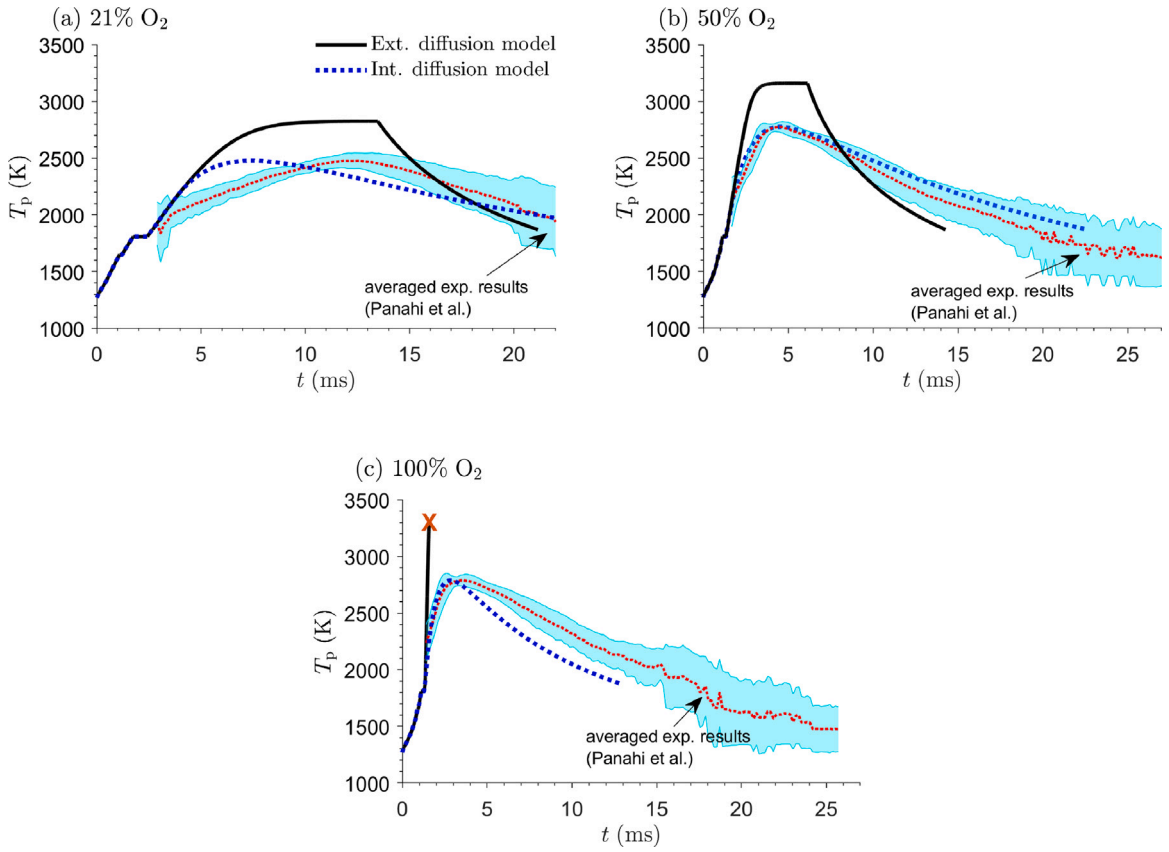

Fig. 14. Time history of particle temperature predicted by model assuming O_2-transport-limited liquid-phase FeO formation (black solid) and the heuristic model considering internal diffusion limiting the rate of oxidation (blue dashed), compared to averaged particle temperature measurements by Panahi et al. [7] (red dotted), and one standard deviation above and below the averaged measurements (light blue band). Plots shown for combustion in (a) air, (b) 50% O_2, and (c) pure O_2. Initial conditions: $d_{p,0} = 42\,\mu m$, $T_g = 1350$ K, with molar fractions (a) $X_{O_2} : X_{N_2} = 0.21 : 0.79$, (b) $X_{O_2} : X_{N_2} = 0.50 : 0.50$, and (c) $X_{O_2} : X_{N_2} = 0.99 : 0.01$. (For interpretation of the references to color in this figure legend, the reader is referred to the web version of this article.)

in the Arrhenius term, slowing the liquid-phase Fe to liquid-phase FeO conversion as the reaction progresses.

Of the two parameters, the pre-exponential factor and the activation temperature, the latter can be empirically determined from experimental work on reaction rate analysis of liquid iron oxidation. Experiments conducted by Banya and Shim [18] explored the rate of liquid iron oxidation via O_2 pressure measurements in a constant volume reaction chamber. Kinetic rate analysis via model fitting showed that the rate of liquid Fe oxidation in the presence of an outer liquid FeO layer was best described by an internal diffusion model through the liquid FeO layer. An apparent activation energy of $20\,920\,J\,mol^{-1}$ was obtained, corresponding to an activation temperature value of 2516 K, which is used for the value of $T_{a,FeO,\ell}$ in the current study. The pre-exponential factor can be calibrated for each experimental measurement such that the peak temperature predicted by the model exhibits good agreement with the experimental peak temperature value.

In this heuristic model considering the internal diffusion during liquid-phase combustion, the rate of liquid-phase Fe oxidation is either external-O_2-transport-limited, or limited by the rate of internal diffusion. In the latter case, an iterative solver is used to calculate the surface O_2 concentration such that the rate of O_2 transport to the particle surface is equal to the rate of O_2 consumption prescribed by the calibrated internal diffusion rate. This ensures that the correct gas composition is used to evaluate boundary-layer-averaged transport properties.

Fig. 12 compares the results considering internal-diffusion-limited combustion to the previous model result assuming entirely O_2-transport-limited combustion in liquid-phase. Fig. 13 plots the rates of heat release and losses (*upper*), as well as the mass transport rate of O_2 to the particle surface and the mole fraction of O_2 at the particle surface (*lower*), for the heuristic model considering internal diffusion kinetics. The pre-exponential factor in Eq. (23) is set to 2.87×10^{-8} $m^2 s^{-1}$, which was iteratively determined such that the heuristic model result matches the experimental peak temperature measurement. While the liquid-phase combustion is initially external-O_2-transport-limited, the internal diffusion becomes rate limiting at around 19 ms, as evident in the heat release rate curve sloping downward in Fig. 13 *upper*. The peak temperature occurs at around 21 ms, shortly after the transition to a kinetically-limited regime. This corresponds to the point in which the heat release rate intersects with the heat loss rate, instead of the point of liquid-phase Fe burnout as seen before. The reaction continues to progress at an increasingly slower rate as the particle cools down to the re-solidification point of Fe_3O_4, giving rise to a "reactive cooling" phenomenon. The surface mole fraction of O_2 approaches that of the bulk gas as the reaction progresses.

The reactive cooling phenomenon is consistent with pyrometric observations by Banya et al. [18],[1] where, during the oxidation of liquid-phase Fe by pure O_2, a sudden temperature increase is recorded as a layer of liquid-phase oxide product rapidly forms, followed by a slow consumption of O_2 while the surface temperature of the metal/oxide sample decreases.

The calibration of the pre-exponential factor is also performed for the high temperature gas combustion cases [7], and results of the two models are compared against experimental measurements in Figs. 14 (a), (b), and (c), for combustion in air, 50% O_2, and pure O_2, respectively. The calibrated pre-exponential factors are summarized in

[1] Note that Ref. [18] is written in Japanese.

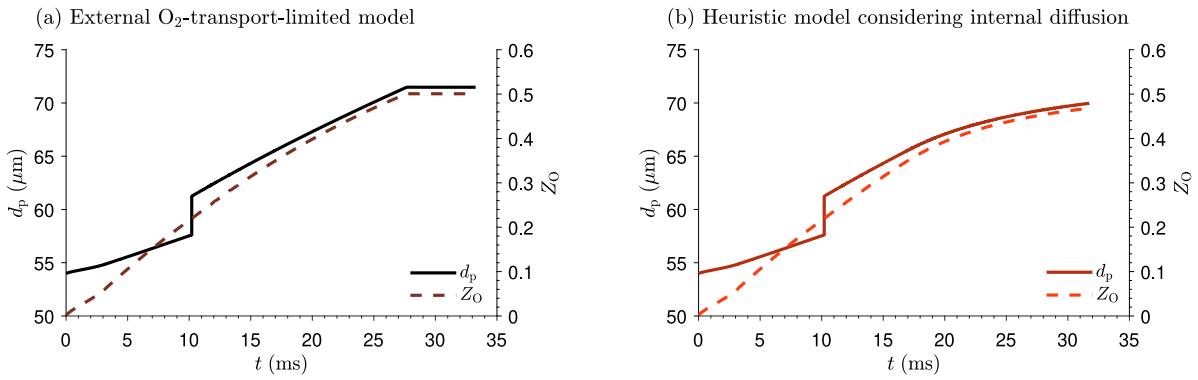

Fig. 15. The time-evolution of particle diameter (*left axis*) and Z_O in the particle (*right axis*) for the model considering (a) external-O_2-transport-limited combustion and the (b) heuristic model considering internal diffusion. Initial conditions: $d_{p,0} = 54\,\mu m$, $T_g = 300$ K, $X_{O_2} : X_{N_2} = 0.21 : 0.79$.

Table 2
Calibrated pre-exponential factors and activation temperature for the kinetics of internal diffusion through a liquid-phase FeO layer.

Experimental data	k_0 ($m^2\ s^{-1}$)
Ning et al. (Air)	2.87×10^{-8}
Panahi et al. (Air)	1.23×10^{-8}
Panahi et al. (50% O_2)	2.23×10^{-8}
Panahi et al. (Pure O_2)	4.97×10^{-8}

Table 2. The calculated mean is 2.83×10^{-8} with a standard deviation of 1.58×10^{-8} with units $m^2 s^{-1}$.

Apart from the case for combustion in air (Fig. 14(a)), the heuristic model considering internal diffusion appears to predict the time to peak temperature with excellent agreement to experimental measurement. The reactive cooling process also renders the rate of cooling much slower than the model considering inert cooling and, generally, shows better agreement with the experimental measurement compared to the model considering only external-O_2-transport-limited combustion. However, it is important to note the discrepancy in the calibrated pre-exponential factors for varying oxygen concentration. This reinforces the understanding that a comprehensive model for single iron particle combustion requires the consideration of internal kinetics that are oxygen concentration-dependent (i.e., surface reactions), and motivates further experimental investigations into the governing physics behind liquid-phase single iron particle combustion.

5.3. Time-evolution of particle size and Z_O

The time evolution of the particle size and Z_O is visualized in Figs. 15, for (a) the external-O_2-transport-limited model, and (b) the heuristic model considering internal diffusion. The sudden jump in particle size at around 10 ms is due to the consideration of the liquid-phase densities of Fe and FeO. The particle size can be seen to increase during the course of the oxidation of iron, due to the fact that its oxide products have a smaller density. While this result is uncertain due to the scattered data on the liquid-phase density of iron oxides at high temperatures, the current model prediction suggests a slight increase in particle size during its combustion lifetime of around 1.30–1.33 times the initial particle size, which is comparable to the *in situ* measurements of particle size upon the first inflation made by Ning et al. [35]. The plots for the case where $T_g = 1350$ K are not included as they are qualitatively similar to Fig. 15, where the particle inflation is around 1.29–1.30 times the initial particle size. Note that the sudden inflation of the particle at the spearpoint is not considered in the current model, as the model simulation is terminated upon reaching the re-solidification temperature of Fe_3O_4. Moreover, other mechanisms of volumetric expansion during the liquid-phase combustion, such as micro-explosions [51], are not considered in the current model.

Note that, in the heuristic model considering internal diffusion, the particle does not reach $Z_O = 0.5$, i.e., some liquid-phase Fe is left in the particle at the time of re-solidification. This is consistent across all test cases (Figs. 12 and 14) considered in this study.

5.4. Effect of particle size and oxidizer concentration on peak temperature

The peak particle temperature of a particle ignited in ambient air is plotted in Fig. 16 as a function of oxygen concentration in the gas for selected initial particle sizes, for two gas temperatures, (a) 300 K and (b) 1350 K. Note that, for the external-O_2-transport-limited model, the simulations are stopped past $X_{O_2} = 0.63$ since the predicted particle temperature exceeds 3280 K.

The model considering a completely external-O_2-transport-limited combustion in liquid-phase predicts that the peak temperature monotonically increases with oxygen concentration. While the Stefan flow effect enhances both O_2 mass transport to the particle as well as the convective heat transfer away from the particle, the increasing oxygen concentration facilitates a faster rate of diffusive oxygen transport to the particle surface, and therefore a faster rate of heat release, while the effect of changing gas composition on the rate of convective heat loss is negligible due to the comparable thermal conductivity of O_2 and N_2. Heat loss due to evaporation of Fe and FeO plays a negligible role in the combustion dynamics for low oxygen concentrations where the peak temperatures are low. As the oxygen concentration is further increased, there is a shallower increase in peak particle temperature, due to the increased significance of heat loss associated with Fe and FeO evaporation.

The heuristic model, considering internal-diffusion-limited combustion, predicts an increasing peak temperature with oxygen concentration up to around $X_{O_2} \approx 0.4$. The peak temperature then plateaus, and does not vary with further increase in oxygen concentration until around $X_{O_2} \approx 0.6$–0.7. An increase in oxygen concentration increases the rate of reaction while the combustion is still external-O_2-transport-limited, which leads to a faster reaction rate and, therefore, faster particle temperature increase. However, this makes the reaction transition to an internal-diffusion-limited regime quicker, due to the rapid consumption of liquid-phase Fe and growth of the layer of $Z_O = 0.5$ oxide product. In addition, the transition to internal-diffusion-limited combustion will occur at a lower temperature, for a faster external O_2 transport rate. These counteracting phenomena lead to the particle reaching a peak at roughly the same temperature despite the increase in oxygen concentration. The peak temperature is then predicted to decrease at very high oxygen concentrations. This arises due to the very rapid O_2 transport rate for high bulk gas oxygen concentrations, which makes the combustion regime transition to internal-diffusion-limited

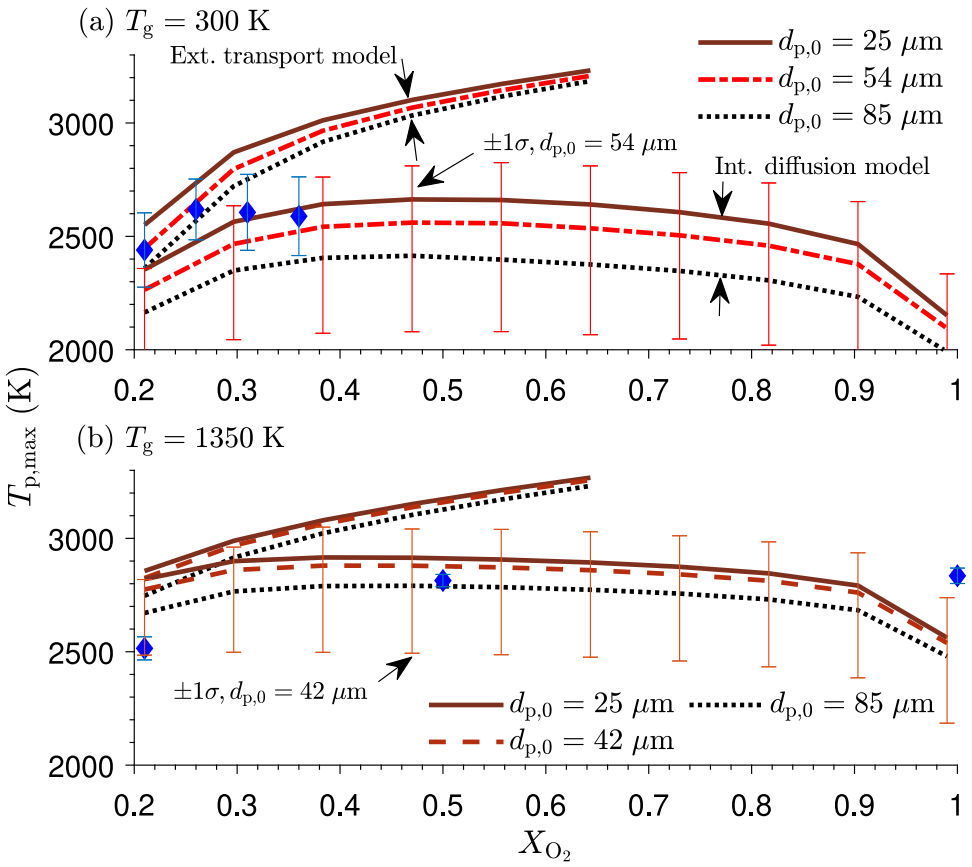

Fig. 16. Maximum particle temperature, $T_{p,max}$, for a single iron particle burning in an O_2/N_2 mixture at gas temperatures (a) T_g = 300 K and (b) T_g = 1350 K, as a function of oxygen concentration X_{O_2} for a range of initial particle sizes $d_{p,0}$. Model results for the external-O_2-transport-limited model, as well as the heuristic model considering internal kinetics, are shown. For the heuristic model considering internal kinetics, the mean pre-exponential factor from values of Table 2 are used. Results for a pre-exponential factor one standard deviation above and below the mean are shown for the (a) $d_{p,0}$ = 54 μm and (b) $d_{p,0}$ = 42 μm. Initial particle temperature is set to $T_{p,0}$ = 1270 K. Experimental data points of peak particle temperature from (a) Ning et al. [6] where $d_{p,0}$ = 54.36 μm and (b) Panahi et al. [7] where $d_{p,0}$ = 38–45 μm are shown in blue, with their respective error bars. (For interpretation of the references to color in this figure legend, the reader is referred to the web version of this article.)

even faster, leading to the heat release rate going below the heat loss rate sooner in the combustion process.

The experimental measurements of peak temperature appear to plateau with increasing oxygen concentration as observed in Fig. 16. While the external-O_2-transport-limited model does not predict this, the heuristic model considering internal diffusion is able to capture a plateauing peak temperature with increasing oxygen concentration, but only up to around $X_{O_2} = 0.7$. The heuristic model considering internal diffusion generally exhibits better agreement with experimental measurement than the model considering external-O_2-transport-limited combustion.

In the same figure, the effect of initial particle size on the peak temperature can be observed, for the external-O_2-transport-limited model and the heuristic model considering internal diffusion, respectively. One consistent pattern is the trend of decreasing peak particle temperature with particle size. This is in contrast to what was reported by Ning et al. [6], where higher peak temperatures were observed for larger particles. Authors of [6] explain this phenomenon as the reduced surface-to-volume ratio of larger particles resulting in a diminishing effect of radiative heat loss with increasing particle size. However, the current model simulations predict the opposite trend. This is likely a result of the slower temperature increase for larger particles stemming from the faster increase in volumetric heat capacity, which scales with $d_{p,0}^3$, than the increase in heat release rate, which scales with $d_{p,0}$. As communicated by the authors of Ref. [6], the peak temperatures as a function of particle size (Fig. 13) report the maximum peak temperatures that were detected in a batch of 10 s of individually burnt particles, rather than the mean peak temperatures of the batch. The error bars provided in the figure indicate the measurement tolerance, rather than a statistical distribution range. The results reported in Part I of the current study do not show the same dependence of peak temperature on particle size. Therefore, based on the uncertainties identified in the present theoretical study, we are inviting the community to further investigate this phenomenon.

6. Discussion

This section discusses possible sources of error in the model that may have led to disagreement between model and experimental measurement, as well as potential future work to mitigate such discrepancies.

6.1. Effect of nanoparticles on gas-phase mass and thermal transport

The current work assumes gas-phase diffusion and inward Stefan-flow to transport O_2 from the bulk gas to the particle surface. While the effect of evaporated gas-phase iron-containing species consuming inward-transported O_2 is considered, there are further complications, that may hinder O_2 transport, which are not considered in the current model development. In particular, the cloud of nanoparticles that surrounds the particle, as observed in experiments [6,7,30,31,52–56], should inhibit the inward transport of O_2. This may also influence the rate of heat removal from the particle, due to an intermediate barrier between the particle and the bulk gas, changing the temperature gradient driving heat loss. A boundary-layer resolved model should be employed to further investigate the validity of the current mass and

thermal transport model across a wide range of gas-phase temperatures and O_2 concentrations.

6.2. Assumption of core and shell geometry

The current model assumes immiscible regions of liquid-phase Fe and FeO in a core and shell configuration during the liquid-phase combustion. This assumption is based on the evidence for physically distinct, immiscible layers of molten oxide and molten Fe in experimental studies on the liquid-phase combustion of liquid iron [26]. However, the validity of this assumption for a micron-sized particle is uncertain, due to the much larger scale of the liquid iron sample used in the experiments in [26]. The morphology of the liquid-phase particle and the species present at the particle surface should be explored further through experimental verification.

6.3. Diffusion coefficients

The diffusion coefficient in Eq. (23) is not empirically determined, but is rather expressed in Arrhenius form where kinetic parameters are calibrated to available experimental measurements. An estimation of the diffusion coefficients of O in an Fe-O mixture using MD simulations would be a valuable extension to the current work, both to provide more physically accurate quantitative data on the kinetics of internal diffusion through liquid-phase iron oxide, and to validate the results presented in this work. Note that, if the diffusion coefficients dictate that the oxygen ions in the Fe-O mixture can diffuse to the core of the particle at a rate comparable to the burning rate of the particle, this may indicate the presence of a continuous gradient of oxygen ion concentration in the liquid-phase particle, instead of distinct regions of liquid-phase Fe and liquid-phase FeO.

6.4. Rate-limiting internal mechanism

The internal transport mechanism considered in the heuristic model presented in Section 5.2 is not the only internal mechanism in the heterogeneous combustion of liquid-phase iron particles that could become rate-limiting. A recent study by Thijs et al. [50] demonstrates that an MD-simulations-informed model, considering the rate of oxidation limited by surface reactions, can achieve better agreement with experimental measurements, compared to a model considering only external O_2 transport to be rate-limiting. Moreover, in addition to the internal diffusion considered in the current work, it is possible that internal convection occurs within the particle, enhancing transport of the reactive Fe and O ions.

While the full picture of the rate-limiting mechanisms in liquid-phase iron particle combustion remains inconclusive, these studies demonstrate the inability of simple external-O_2-transport-limited models to accurately model the single particle combustion process. The fact that the consideration of internal transport limitations improves the accuracy of such simulation results continues to motivate further experimental studies on the fundamental mechanisms behind liquid-phase iron particle combustion, as well as particle-resolved modeling work to investigate the physics of internal iron oxidation mechanisms.

7. Concluding remarks

A theoretical framework for the solid-to-liquid phase transition and the subsequent liquid-phase combustion of a single iron particle was developed. A zero-dimensional model was constructed based on the simplifying assumption of rapid internal kinetic processes, such that the overall rate of combustion in liquid-phase is dictated by the rate of external O_2 transport. The model considered a particle structure wherein a shell of liquid-phase FeO encloses a core of liquid-phase Fe. The gas-phase transport consisting of O_2 diffusion and convection (via Stefan flow) toward the particle surface and evaporated Fe and FeO diffusion away from the particle surface was considered. The outward-transported gas-phase Fe and FeO were modeled to inhibit the heat release rate of the condensed-phase particle, as they consume inward-transported O_2 stoichiometrically to condense into Fe_2O_3 nanoparticles. The current model considering only external-O_2-transport-limited combustion was compared to experimental measurements on single iron particle combustion in ambient temperature air, as well as at high gas temperatures in varying oxygen concentrations. Comparisons show consistent overprediction of the peak particle temperature, revealing that the assumption of rapid internal kinetics may not be accurate. The calculated rate of inert particle cooling also overpredicted the rate of particle cooling observed in experimental measurements. A further analysis via a heuristic model was proposed, considering internal-diffusion-limited combustion. Calibration of the pre-exponential factor to match the experimental peak temperature improves the agreement between model and experiment for both time to peak temperature and the particle cooling rate. A plateau in peak temperature with increasing oxygen concentration was observed when the internal diffusion is considered. Future work should focus on elucidating the internal physical mechanisms that become rate-limiting, as well as the oxidation mechanisms during, and after, the re-solidification of the liquid-phase particle.

Declaration of competing interest

The authors declare that they have no known competing financial interests or personal relationships that could have appeared to influence the work reported in this paper.

Data availability

Data will be made available on request.

Acknowledgments

The authors thank D. Ning for providing experimental data for comparison. This project is undertaken with the financial support of the Canadian Space Agency, Canada; McGill Sustainability Systems Initiative (MSSI); Northeastern University, USA; Ruhr University Research 520 School PLUS; the Natural Sciences and Engineering Research Council of Canada, Canada. LCT was supported by the European Research Council (ERC) under the European Union's Horizon 2020 research and innovation programme under Grant Agreement no. 884916.

References

[1] Beach D, Rondinone AJ, Sumpter B, Labinov S, Richards R. Solid-state combustion of metallic nanoparticles: New possibilities for an alternative energy carrier. J Energy Resour Technol 2006;129(1):29–32.
[2] Bergthorson JM, Goroshin S, Soo MJ, Julien P, Palecka J, Frost DL, et al. Direct combustion of recyclable metal fuels for zero-carbon heat and power. Appl Energy 2015;160:368–82.
[3] Bergthorson JM. Recyclable metal fuels for clean and compact zero-carbon power. Prog Energy Combust Sci 2018;68:169–96.
[4] Debiagi P, Rocha R, Scholtissek A, Janicka J, Hasse C. Iron as a sustainable chemical carrier of renewable energy: Analysis of opportunities and challenges for retrofitting coal-fired power plants. Renew Sustain Energy Rev 2022;165:112579.
[5] Kuhn C, Düll A, Rohlfs P, Tischer S, Börnhorst M, Deutschmann O. Iron as recyclable energy carrier: Feasibility study and kinetic analysis of iron oxide reduction. Appl Energy Combust Sci 2022;12:100096.
[6] Ning D, Shoshin Y, van Stiphout M, van Oijen JA, Finotello G, de Goey LPH. Temperature and phase transitions of laser-ignited single iron particle. Combust Flame 2022;236:421–32.
[7] Panahi A, Chang D, Schiemann M, Fujinawa A, Mi X, Bergthorson JM, et al. Combustion behavior of single iron particles-part I: An experimental study in a drop-tube furnace under high heating rates and high temperatures. Appl Energy Combust Sci 2023;13:100097.
[8] Païdassi J. Sur la cinetique de l'oxydation du fer dans l'air dans l'intervalle 700–1250 C. Acta Metall 1958;6(3):184–94.
[9] Hauffe K. The mechanism of oxidation of metals—Theory. In: Oxidation of metals. Boston, MA: Springer US; 1965, p. 79–143.

[10] Goursat A, Smeltzer W. Kinetics and morphological development of the oxide scale on iron at high temperatures in oxygen at low pressure. Oxid Met 1973;6(2):101–16.
[11] Garnaud G, Rapp R. Thickness of the oxide layers formed during the oxidation of iron. Oxid Met 1977;11(4):193–8.
[12] Atkinson A. Transport processes during the growth of oxide films at elevated temperature. Rev Modern Phys 1985;57:437–70.
[13] Chen R, Yeun W. Review of the high-temperature oxidation of iron and carbon steels in air or oxygen. Oxid Met 2003;59(5):433–68.
[14] Mi X, Fujinawa A, Bergthorson JM. A quantitative analysis of the ignition characteristics of fine iron particles. Combust Flame 2022;240(112011).
[15] Jean-Philyppe J, Fujinawa A, Bergthorson J, Mi X. The ignition of fine iron particles in the Knudsen transition regime. Combust Flame 2023. Accepted.
[16] Goroshin S, Palečka J, Bergthorson JM. Some fundamental aspects of laminar flames in nonvolatile solid fuel suspensions. Prog Energy Combust Sci 2022;91:100994.
[17] Emi T, Boorstein W, Pehlke R. Absorption of gaseous oxygen by liquid iron. Metall Mater Trans B 1974;5:1959–66.
[18] Banya S, Shim J-D. Rate of oxidation of liquid iron by pure oxygen. Tetsu Hagane 1980;66:1631–9.
[19] Sato J, Sato K, Hirano T. Fire spread mechanisms along steel cylinders in high pressure oxygen. Combust Flame 1983;51:279–87.
[20] Ward NR, Steinberg TA. The rate-limiting mechanism for the heterogeneous burning of cylindrical iron rods. J ASTM Int 2009;6(6):1–13.
[21] Hirano T, Sato K, Sato Y, Sato J. Prediction of metal fire spread in high pressure oxygen. Combust Sci Technol 1983;32(1–4):137–59.
[22] Steinberg TA, Mulholland GP, Wilson DB, Benz FJ. The combustion of iron in high-pressure oxygen. Combust Flame 1992;89(2):221–8.
[23] Steinberg TA, Kurtz J, Wilson DB. The solubility of oxygen in liquid iron oxide during the combustion of iron rods in high-pressure oxygen. Combust Flame 1998;113(1):27–37.
[24] Dreizin EL. Phase changes in metal combustion. Prog Energy Combust Sci 2000;26(1):57–78.
[25] Wilson DB, Steinberg TA, Stoltzfus JM. Thermodynamics and kinetics of burning iron. Flammabl Sensit Mater Oxyg Enrich Atmospheres 1997;8:240–57.
[26] Muller M, El-Rabii H, Fabbro R. Liquid phase combustion of iron in an oxygen atmosphere. J Mater Sci 2015;50(9):3337–50.
[27] Ning D. Experimental investigation into single iron particle combustion [Ph.D. thesis], Eindhoven University of Technology; 2022.
[28] Choisez L, van Rooij NE, Hessels CJM, da Silva AK, Filho IRS, Ma Y, de Goey LPH, Springer H, Raabe D. Phase transformations and microstructure evolution during combustion of iron powder. Acta Mater 2022;239:118261.
[29] Nelson LS. Nature of the spearpoints observed during the combustion of zirconium droplets. Nature 1965;207:741.
[30] Tóth P, Ögren Y, Sepman A, Gren P, Wiinikka H. Combustion behavior of pulverized sponge iron as a recyclable electrofuel. Powder Technol 2020;373:210–9.
[31] Ning D, Shoshin Y, van Oijen JA, Finotello G, de Goey LPH. Burn time and combustion regime of laser-ignited single iron particle. Combust Flame 2021;230:111424.
[32] Huang J, Li S, Cai W, Qian Y, Berrocal E, Aldén M, et al. Quantification of the size, 3D location and velocity of burning iron particles in premixed methane flames using high-speed digital in-line holography. Combust Flame 2021;230:111430.
[33] Philibert J, Vignes A, Bréchet Y, Combrade P. Métallurgie - 2ème édition: Du minerai au matériau. Dunod; 2002.
[34] Palečka J, Goroshin S, Higgins AJ, Shoshin Y, de Goey LPH, Angilella J-R, et al. Percolating reaction–diffusion waves (PERWAVES)—Sounding rocket combustion experiments. Acta Astronaut 2020;177:639–51.
[35] Ning D, Shoshin Y, van Oijen JA, Finotello G, de Goey LPH. Size evolution during laser-ignited single iron particle combustion. Proc Combust Inst 2022.
[36] Soo MJ, Mi X, Goroshin S, Higgins AJ, Bergthorson JM. Combustion of particles, agglomerates, and suspensions -A basic thermophysical analysis. Combust Flame 2018;192:384–400.
[37] Wlokas I, Faccinetto A, Tribalet B, Schulz C, Kempf A. Mechanism of iron oxide formation from iron pentacarbonyl-doped low-pressure hydrogen/oxygen flames. Int J Chem Kinet 2013;45(8):487–98.
[38] Cifuentes L, Sellmann J, Wlokas I, Kempf A. Direct numerical simulations of nanoparticle formation in premixed and non-premixed flame–vortex interactions. Phys Fluids 2020;32(9):093605.
[39] Nanjaiah M, Pilipodi-Best A, Lalanne MR, Fjodorow P, Schulz C, Cheskis S, et al. Experimental and numerical investigation of iron-doped flames: FeO formation and impact on flame temperature. Proc Combust Inst 2021;38(1):1249–57.
[40] Rahinov I, Sellmann J, Lalanne MR, Nanjaiah M, Dreier T, Cheskis S, et al. Insights into the mechanism of combustion synthesis of iron oxide nanoparticles gained by laser diagnostics, mass spectrometry, and numerical simulations: A mini-review. Energy Fuels 2021;35(1):137–60.
[41] McBride B. Coefficients for calculating thermodynamic and transport properties of individual species, vol. 4513. NASA Langley Research Center; 1993.
[42] Thijs LC, van Gool CEAG, Ramaekers WJS, Kuerten JGM, van Oijen JA, de Goey LPH. Improvement of heat- and mass transfer modeling for single iron particles combustion using resolved simulations. Combust Sci Technol 2022;1–17.
[43] Crowe CT, Schwarzkopf JD, Sommerfeld M, Tsuji Y. Multiphase flows with droplets and particles. CRC Press; 2011.
[44] Thijs LC, van Gool CEAG, Ramaekers WJS, van Oijen JA, de Goey LPH. Resolved simulations of single iron particle combustion and the release of nano-particles. Proc Combust Inst 2022.
[45] Rumminger M, Reinelt D, Babushok V, Linteris G. Numerical study of the inhibition of premixed and diffusion flames by iron pentacarbonyl. Combust Flame 1999;116(1):207–19.
[46] Kirshenbaum AD, Cahill JA. The density of liquid iron from the melting point to 2500 K. Trans Met Soc AIME 1962;224.
[47] Millot F, Rifflet J, Wille G, Sarou-Kanian V. Density and surface tension of liquid iron oxides. High Temp - High Press 2008;38(3):245–57.
[48] Chase M. NIST-JANAF thermochemical tables. 4th ed. American Institute of Physics, -1; 1998.
[49] Dreizin EL, Suslov AV, Trunov MA. General trends in metal particles heterogeneous combustion. Combust Sci Technol 1993;90(1–4):79–99.
[50] Thijs L, Kritikos E, Giusti A, Ramaekers W, van Oijen J, de Goey L, Mi X. On the surface chemisorption of oxidizing fine iron particles: insights gained from molecular dynamics simulations. Combust Flame 2023. Accepted.
[51] Li T, Heck F, Reinauer F, Böhm B, Dreizler A. Visualizing particle melting and nanoparticle formation during single iron particle oxidation with multi-parameter optical diagnostics. Combust Flame 2022;245:112357.
[52] McRae M, Julien P, Salvo S, Goroshin S, Frost DL, Bergthorson JM. Stabilized, flat iron flames on a hot counterflow burner. Proc Combust Inst 2018.
[53] Palečka J, Sniatowsky J, Goroshin S, Higgins AJ, Bergthorson JM. A new kind of flame: Observation of the discrete flame propagation regime in iron particle suspensions in microgravity. Combust Flame 2019;209:180–6.
[54] Poletaev N, Khlebnikova M. Combustion of iron particles suspension in laminar premixed and diffusion flames. Combust Sci Technol 2020;1–22.
[55] Li S, Sanned D, Huang J, Berrocal E, Cai W, Aldén M, et al. Stereoscopic high-speed imaging of iron microexplosions and nanoparticle-release. Opt Express 2021;29(21):34465–76.
[56] Li S, Huang J, Weng W, Qian Y, Lu X, Aldén M, et al. Ignition and combustion behavior of single micron-sized iron particle in hot gas flow. Combust Flame 2022;241:112099.